DIPLOMARBEIT

Surface Characterization of In_2O_3(001) Single Crystals

Ausgeführt am Institut für Angewandte Physik
der Technischen Universität Wien

Unter der Anleitung von
Univ.Prof. Dipl.-Ing. Dr.techn. Ulrike Diebold

durch

Manfred Menhart

Favoritenstraße 119/2/9
1100 Wien

Wien, am 26. März 2012 _____

Kurzfassung

Indiumoxid (In_2O_3) ist seit langer Zeit Gegenstand wissenschaftlicher Forschung. Es ist ein transparenter Halbleiter, der sich in vielen technischen Anwendungen wie zum Beispiel organischen Leuchtdioden (OLEDs - Organic Light Emitting Diodes), organischen Solarzellen (OPVCs - Organic Photovoltaic Cells) und transparenten Infrarotreflektoren wiederfindet. Diese Diplomarbeit setzt Daniel Hagleitners Arbeit an hochqualitativen $In_2O_3(001)$ Einkristallen fort [1, 2]. Eine Serie von Proben, die unter unterschiedlichen Zusammensetzungen von Flussmitteln - beigefügte BaO, CaO und MgO Zusätze in unterschiedlicher Dosierung - gewachsen wurden, werden mittels Oberflächen- und Festkörperanalysemethoden verglichen. Massenspektrometrie mit induktiv gekoppeltem Plasma (ICP-MS - Inductively Coupled Plasma Mass Spectrometry) gibt Aufschluss über die in den Kristallen eingebetteten Elemente. Unter reduzierenden Bedingungen bestätigen Augerelektronenspektroskopie (AES) und niederenergetische Ionenstreuspektroskopie (LEIS - Low-Energy Ion Scattering Spectroscopy) Indium Kristalloberflächen bei allen Proben, während Rastertunnelmikroskopie (STM - Scanning Tunneling Microscope) geringfügige Unterschiede in der Oberflächenstruktur zeigt. Alle untersuchten Einkristalle haben gewisse Grundzüge wie durchgängig 5 Å hohe Stufenkanten und atomare Cluster auf einem 2.5 Å tiefer liegenden Gitter gemeinsam, wobei sich die verschiedenen Proben durch Terrassengrößen und die Anordnung der Atomcluster auf der obersten Lage voneinander unterscheiden. Ladungsträgerkonzentration und elektrischer Widerstand Hagleitners Kristalls werden mittels Hallmessungen zu $n \approx 3 \times 10^{14}$ cm^{-3} und $\rho = 1.044 \times 10^5$ Ω·cm korrigiert, was noch immer ein bemerkenswertes Ergebnis darstellt. Die Werte für andere Kristalle ähnlicher Zusammensetzung liegen in der Größenordnung bisher gefundener Werte. Weiters wird der Einfluss von atomarem Sauerstoff, atomarem Wasserstoff und molekularem Wasser auf die $In_2O_3(001)$ Oberfläche geprüft und diskutiert.

Abstract

Indium oxide (In_2O_3) has been subject to research for many years. It is a transparent semiconductor that is found in many technical applications like Organic Light Emitting Diodes (OLEDs), Organic Photovoltaic Cells (OPVCs) and transparent infrared reflectors. This thesis continues the work of Daniel Hagleiter on high-quality $In_2O_3(001)$ single crystals [1, 2]. A series of flux grown samples with a variety of flux compositions, namely BaO, CaO, and MgO additives, were investigated by means of surface and bulk analysis techniques. With the results of Inductively Coupled Plasma Mass Spectrometry (ICP-MS), the residual flux elements are compared to the growth parameters. Auger Electron Spectroscopy (AES) and Low-Energy Ion Scattering (LEIS) confirm indium terminated surfaces on all samples, while Scanning Tunneling Microscopy (STM) shows slight differences in the surface structures. Although all crystals share basic features such as consistent 5 Å high step edges and atomic clusters on a 2.5 Å deeper lying sublattice, terrace sizes and the ordering of surface atom clustering distinguish the different samples. Carrier concentration and electric resistivity for Hagleitner's crystal were revised to $n \approx 3 \times 10^{14}$ cm^{-3} and $\rho = 1.044 \times 10^5$ Ω·cm via Hall measurements, which is still a remarkable result. Values for other crystals grown in a similar fashion show results comparable to literature for most crystals. Furthermore the influence of atomic oxygen, atomic hydrogen, and molecular water on the $In_2O_3(001)$ surface is investigated and discussed.

Contents

Acronyms

AES	Auger Electron Spectroscopy
APPH	Auger Peak to Peak Height
DFT	Density Functional Theory
ESCA	Electron Spectroscopy for Chemical Analysis
ICP-MS	Inductively Coupled Plasma Mass Spectrometry
ISS	Ion Scattering Spectroscopy
ITO	Indium Tin Oxide
LEED	Low-Energy Electron Diffraction
LEIS	Low-Energy Ion Scattering
OLED	Organic Light Emitting Diode
OPVC	Organic Photovoltaic Cells
PES	Photoelectron Spectroscopy
RT	Room Temperature
STM	Scanning Tunneling Microscope
STS	Scanning Tunneling Spectroscopy
TCO	Transparent Conducting Oxide
ThC	Thermal Cracker
UHV	Ultra-High Vacuum
VdP	Van der Pauw
XPS	X-ray Photoelectron Spectroscopy

1 Indium Oxide In_2O_3

1.1 Introduction

Indium oxide, In_2O_3, is a transparent conductor that has been subject to research for many years. Doped with SnO_2 it is referred to as Indium Tin Oxide (ITO), the standard for Transparent Conducting Oxides. TCOs combine high optical transparency in the visible range with conductivities approaching that of a metal [3]. Naturally, these characteristics lead to many technical applications such as transparent films for organic Light Emitting Diodes (OLEDs), Organic Photovoltaic Cells (OPVCs) and transparent infrared reflectors. Furthermore, indium oxide is used in heterogeneous catalysis [4] and chemical gas sensing [5].

Fundamental research on ITO or pure In_2O_3 is essential because even basic characteristics are controversially discussed [6] and the surface termination of pure indium oxide is not yet sufficiently studied. The polarity of the crystal stacks leads to reconstructions on the surface counteracting the net dipole moment [7]. Density Functional Theory (DFT) calculations suggest possible surface topologies [8], which need to be examined experimentally.

A major problem of previous investigations was the quality of the samples, which were mostly produced by magnetron sputtering, evaporation, or by pressing pellets of powder which usually leads to polycrystalline, highly defective samples [9]. Research on epitaxially-grown In_2O_3 and ITO thin films lead to many new findings [6, 10, 11, 12]. Lately high-quality, (001) oriented single crystals grown with the flux method were investigated by Daniel Hagleitner [1, 2] and the combined results of his work and this thesis are in press for being published in Physical Review B [13]. This thesis continues Hagleitner's research, investigates a variety of differently grown $In_2O_3(001)$ single crystals, and focuses on the surface topology under different treatments.

1.2 Crystal Growth

Flux Method The substances of the desired composition are dissolved in a non-reactive crucible using solvents (flux) at temperatures just above the saturation temperature. The crucible is then slowly cooled down, allowing the crystal to assemble itself, growing to a single crystal of typically a few millimeter in size.

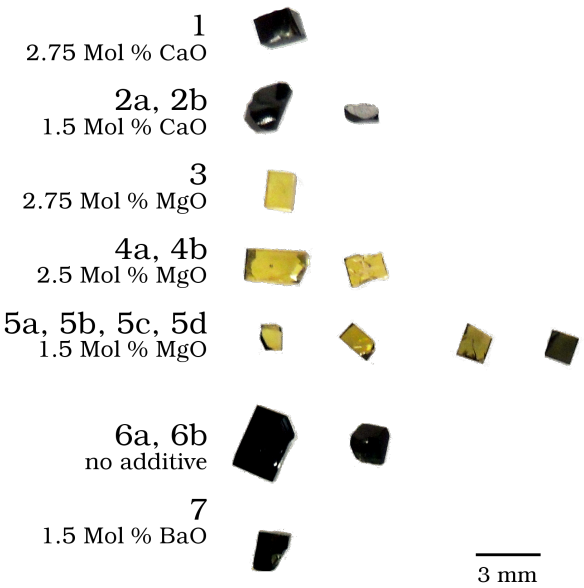

Figure 1.1: *Crystals used for ICP-MS. Crystals from batch 2b, 5b, 6b, and 7 were analyzed by AES, LEIS, and STM. A sample from batch 6b was investigated with LEED, STM, and XPS after surface treatment with oxygen, hydrogen, and water. Hall measurements were performed on samples from batch 2a and 5d. A detailed description of the samples is found in table A.1.*

Samples The samples analyzed in this thesis were grown by Professor Lynn A. Boatner at Oak Ridge National Laboratory (ORNL), USA, using different compositions for the flux. The main part was In_2O_3, B_2O_3, and PbO with additional MgO, CaO, or BaO. Powders of these ingredients were melted in a platinum crucible and held at 1200 °C for 4 to 10 hours. The temperature was decreased by 3 °C per hour until 500 °C was reached and the furnace was turned off. The crystals were removed from the flux using a 1:4 solution of HNO_3 and water [14]. The resulting samples vary from black to transparent yellow, where the most transparent and thus most promising samples were grown with MgO additive. Therefore the focus of this thesis lies on these crystals. A complete list of the samples and their compositions is found in table A.1 and a few of them are shown in figure 1.1.

1.3 Crystal Structure

In normal conditions (below 65 kbar and 1000 °C) In_2O_3 crystallizes in the bixbyite structure (space group $Ia\overline{3}$). This structure is often described as a 2×2×2 fluorite lattice. It is obtained by removing 12 anions from the anion sublattice. Each {100} anion layer contains four vacant positions compared to the fluorite lattice [15]. The previously accepted lattice constant of 10.117 Å was revised to 10.1150(5) Å in the preceding diploma thesis [1] and is soon to be published in Physical Review B [13].

A unit cell consists of 80 atoms: 48 oxygen atoms and 32 indium atoms. There are two types of indium sites that differ in their symmetry which are commonly referred to as In-b and In-d (figure 1.3). Eight indium atoms sit at the more regularly coordinated In-b sites and 24 indium atoms occupy the In-d sites. Along the (001) direction the crystal is a stack of three different layers. The so called D-layer consists of only In-d atoms whereas the M-layer consists of both In-d and In-b atoms. The indium layers are separated by layers of oxygen atoms (see figure 1.2).

The alternating of positive and negative charged layers leads to a net dipole moment perpendicular to the (001) surface (Tasker type-III [7, 16]). As a consequence, the surface cannot have bulklike terminations because the surface of the crystal would be polar and the electrostatic potential would diverge. There are several mechanisms that could lead to stabilization of the surface: Reduction of top and bottom layer surface charges, changes in surface stoichiometry, surface reconstructions, adsorption, or faceting [7].

Indium oxide can also exist in two other forms. The bixbyite structure

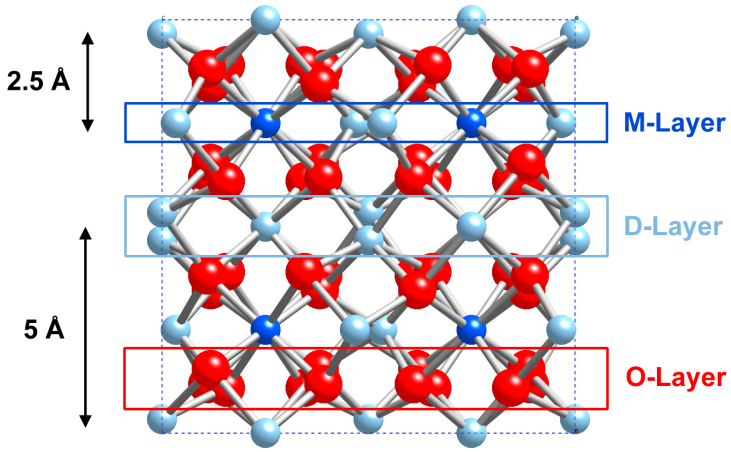

Figure 1.2: *In_2O_3 bixbyite structure (Figure from reference [1]). Red spheres represent oxygen atoms, dark blue In-d, and light blue In-b atoms. There are 3 types of layers: O-layers consisting only of oxygen atoms, D-layers consisting of In-d atoms and M-layers consisting of In-b and In-d atoms.*

of In_2O_3 is transformed to the corundum structure at 65 kbar and 1000 °C. At 111 kbar and 1100 °C it crystallizes in a perovskite-like structure, where In^{+3} occupies both the A and B sites [17, 18, 19]. Both these structures are metastable and annealing at 1200 °C or 800 °C leads to transformations back to the bixbyite structure [18, 19, 20].

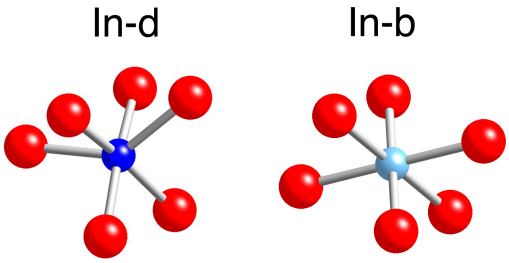

Figure 1.3: *In-d and In-b sites (Figure from reference [1]).*

1.4 Previous Work

1.4.1 Surface Termination According to DFT Simulations

Agoston and Albe [8] conducted fundamental DFT-simulations concerning possible surface terminations for indium oxide. The surface energies of stoichiometric In_2O_3 shows the order (111) < (011) < (211) < (001) for the different orientations, which is in agreement with the results of Walsh et al. [3]. Although the (001) surface is the least favorable, it is often observed experimentally and solely investigated in this thesis.

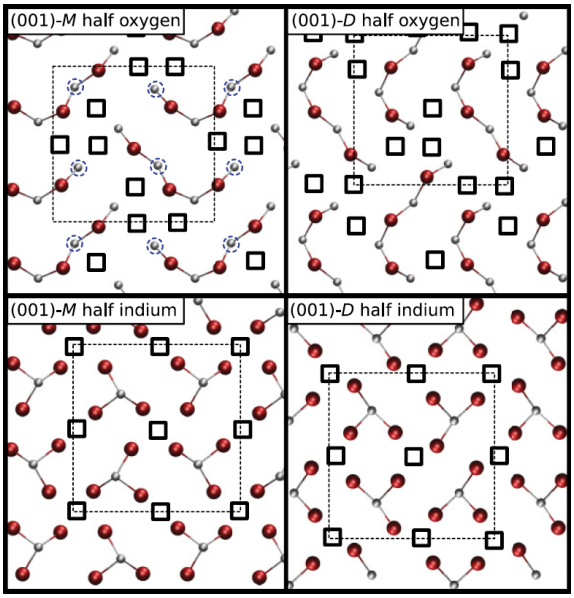

Figure 1.4: *DFT-simulated stoichiometric half-oxygen and half-indium termination for M-layer and D-layer (Figure from reference [8]). Large red balls represent oxygen and small gray balls represent indium. Empty lattice sites are represented by black boxes, In-b atoms are encircled blue.*

For the In_2O_3 (001) surface Agoston and Albe [8] concluded that the stable stoichiometric surface consists mainly of half-filled oxygen planes involving considerable disorder due to low energy differences compared to half-indium terminations ($\Delta E \sim 0.02$ eV/Å^2). For the oxygen surface a (001-D) layer is favorable as the terminal cation layer ($\Delta E \sim 0.011$ eV/Å^2), whereas for half-indium terminations a (001-M) layer is preferred ($\Delta E \sim 0.016$ eV/Å^2). It is also implied that areas of both, half-indium and half-

oxygen could exist and the (001) surface is unstable in respect to faceting into (011) and (111) surfaces.

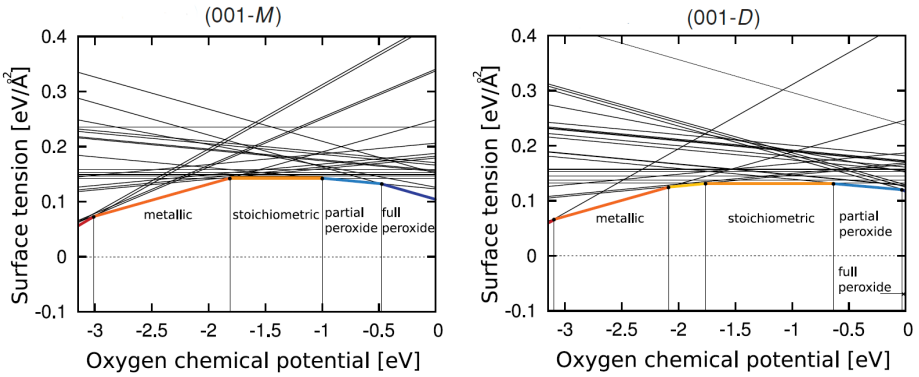

Figure 1.5: *Surface energy as a function of the oxygen chemical potential for the In_2O_3(001) M- and D-layer (Figure from reference [8]).*

Agoston and Albe [8] also investigated variations in stoichiometry under changing chemical environments. The surface energy was calculated as a function of the oxygen chemical potential representing highly reducing to highly oxidizing environments. The resulting diagrams are shown in figure 1.5. Under reducing conditions the most favorable surface is a complete indium termination with all surface oxygen removed. At the lowest oxygen chemical potential additional indium nucleates on the surface leading to an even stronger cation terminated surface. In highly oxidizing environments, for the M-layer as terminating cation layer, dimerization of all oxygen atoms occurs (six dimers per unit cell). A full peroxide surface is not stable for the D-layer termination due to geometric reasons. Between the stoichiometric and the full peroxide surface, another stable state exists for both, D- and M-layers: A partially dimerized surface consisting of four oxide anions and two dimers per unit cell. Figure 1.6 shows the expected surfaces for metallic and peroxide terminations and figure 1.7 shows simulated STM images for different In_2O_3(001) terminations.

Furthermore, the influence of water and hydrogen on the surface was investigated by Agoston and Albe [8]. When water or hydrogen is brought into contact with the In_2O_3(001) surface (by adding one monolayer of water to the stoichiometric surface or dissociating a hydrogen molecule on each dimer of the peroxide surface), it can react and form surface states that

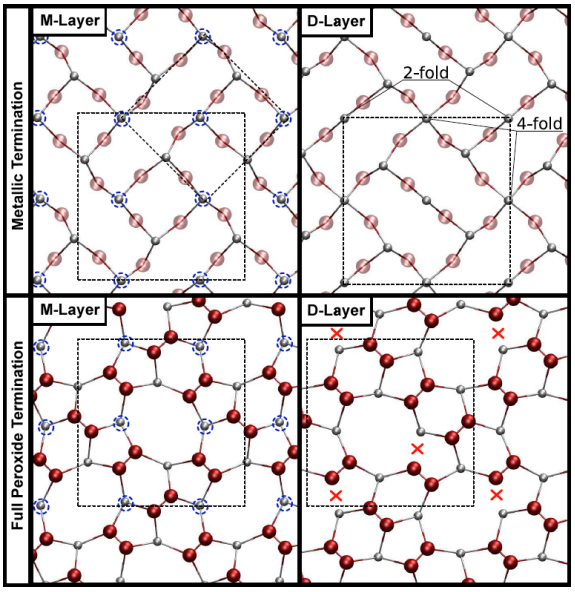

Figure 1.6: *Expected surface for metallic and peroxide terminations (Figure from reference [8]).*

compete with former stable states. In figure 1.8 phase diagrams for the M- and D-layers of the $In_2O_3(001)$ surface are shown in respect to the oxygen chemical potential for the clean and for hydrogenated surfaces, respectively. The hydrogenated surface is most stable and energetically even preferred to the (111) surface (also shown in figure 1.8). For complete removal of water from the surface, its chemical potential has to be set to $\mu_{H_2O} \geq$ -2.6 eV which corresponds to annealing at $\sim$580 K.

1.4.2 Experimental Findings

Despite the wide range of applications for indium oxide, especially Indium Tin Oxide (ITO), very little is known about its fundamental properties. Morales and Diebold [11] investigated the surface of Sn-doped $In_2O_3(001)$ thin films in highly oxidizing environments using LEED and STM techniques. The results are in good agreement with DFT calculations [21, 22], which predict dimerization of the surface oxygen. The concentration of surface dimers is a function of Sn doping, which indicates that addition of Sn effects the electronic, optical, and surface properties of indium oxide thin films.

Hagleitner [1] analyzed flux-grown $In_2O_3(001)$ surfaces by STM, STS,

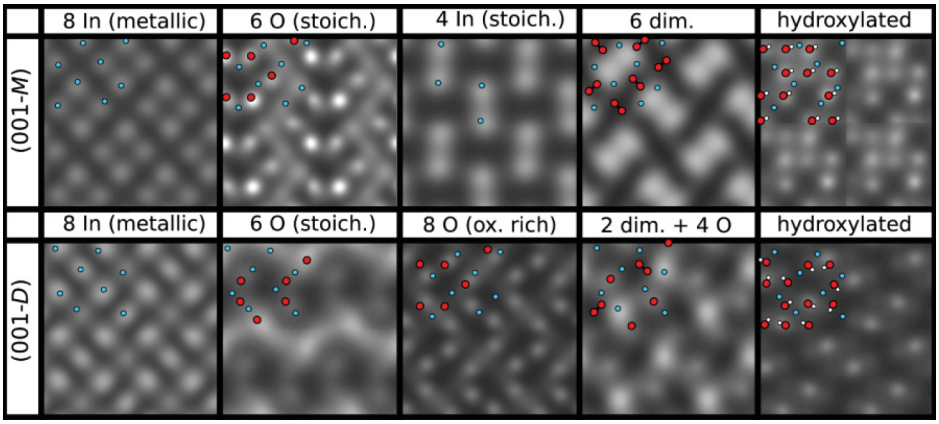

Figure 1.7: *Simulated STM images for different In_2O_3 (001) terminations (Figure from reference [8]).*

and PES. The obtained STM data indicates indium terminated surfaces with large terraces and step edges of 5 Å only. This height corresponds to the distance between identical planes, which means that there is just one termination (M-layer or D-layer) instead of the possible mixed surfaces anticipated by Agoston and Albe [8]. The terraces are covered with 2.5 Å high atomic sized features. Hagleitner explains these features as small "patches" of D-layer atoms on top of an M-layer. Oxidizing the surface lead to smaller terraces and heavy distortion, while the first attempts of dosing water showed no significant changes.

1.4.3 Conductivity of In_2O_3

In_2O_3 is an n-type semiconductor [23, 24], where the conduction is caused by intrinsic donor defects [25]. A relation between oxygen environment and conductivity is repeatedly reported in literature [23, 24, 20, 26]. De Wit [25] suggested oxygen vacancies as dominating ionic defects responsible for high carrier concentration and thus good conductivity even without extrinsic dopants. Tomita et al. [27] on the other hand ruled out oxygen vacancies as native donors and suggested interstitial indium (in coexistence with oxygen vacancies) to be the cause for conducting indium oxide.

Lany and Zunger [28] calculated oxygen vacancy concentrations in the range of 10^{20} cm^{-3} and 10^{7} cm^{-3} for indium interstitials but only low electron densities ($n \leq 10^{7}$ cm^{-3}) at room temperature. They concluded that

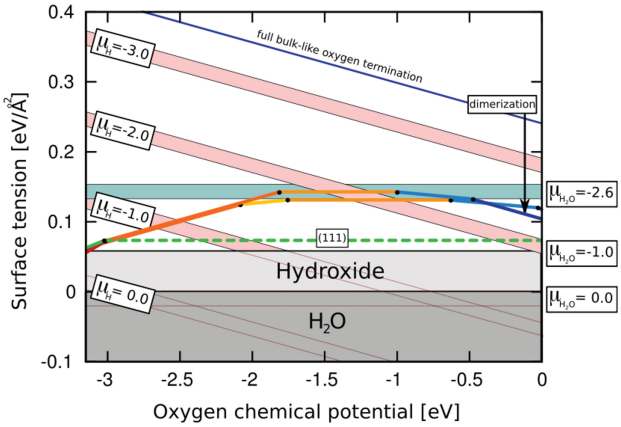

Figure 1.8: *Phase diagram of the In_2O_3(001) surface including hydrogenated surfaces at different isovalues of hydrogen and water chemical potentials (Figure from reference [8]). The bars correspond to the surface energy differences between M- and D-layers.*

intrinsic defects cannot cause n-type conductivity under equilibrium conditions (though pronounced reduction of the band gap explains the rise in electron concentrations at elevated temperatures). Residual conductivity of pure indium oxide could arise from photoconductivity of excited oxygen vacancies.

Experimental values for carrier concentrations lead to values in the order of magnitude of 2×10^{19} cm^{-3} [25] and resistivities ranging from 10^{-4} Ω·m on the opaque metallic crystal to 5×10^{-6} Ω·m for the transparent conducting phase and an insulating transparent phase as the oxygen vacancies are removed [29]. Recent results show a far lower number of charge carriers for high-purity indium oxide single crystals. The measured resistivity of $\rho = 2 \times 10^5$ Ω·cm estimates electron concentrations of n = 1×10^{12} cm^{-3} [2].

2 Experimental Methods

2.1 UHV Systems

The experiments were conducted in two different Ultra-High Vacuum (UHV) chambers. Basic analysis of four In_2O_3 compositions was conducted in the so called Room Temperature STM. Detailed investigation of In_2O_3 with magnesium additive was done in the Omega Laboratory. The names are slightly misleading because both chambers operate at room temperature.

2.1.1 Room Temperature STM Laboratory

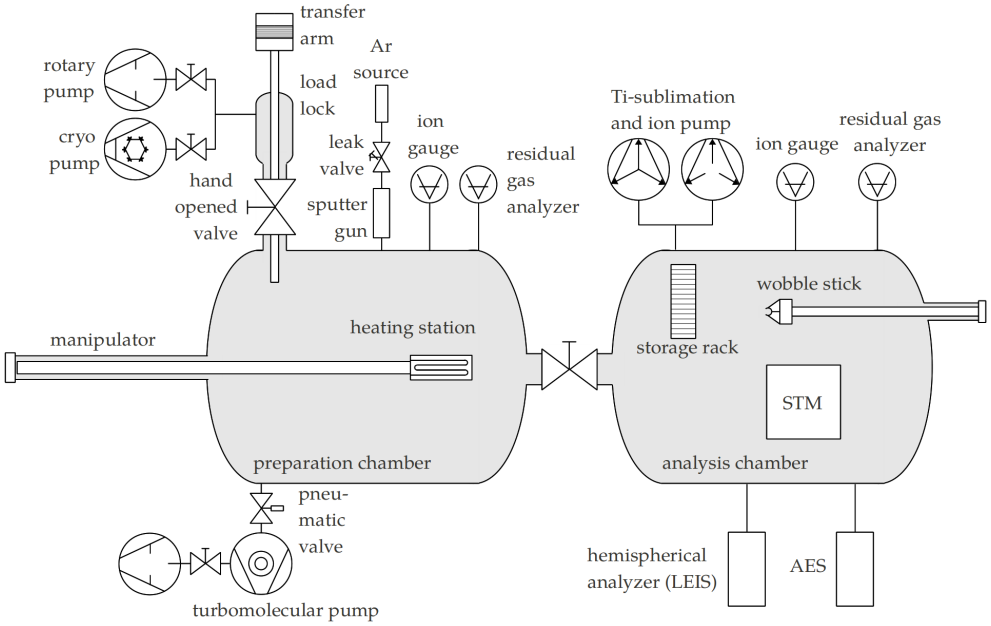

Figure 2.1: *Schematic drawing for the Room Temperature chamber (Figure adapted from reference [30]).*

The system consists of two chambers, the preparation chamber and the analysis chamber. The preparation chamber is held at a pressure below 10^{-10} mbar by a turbomolecular pump supported by a rotary vane pump. Crystals can be sputtered and annealed at the manipulator and the (residual) pressure is monitored by an ion gauge and a residual gas analyzer. Samples can be

inserted into and removed from the preparation chamber one at a time via the load lock, which is a small vacuum chamber pumped by a cryo pump when needed.

The system is capable of AES, LEIS and STM, all operating in the analysis chamber. UHV of down to 3×10^{-11} mbar is reached by an ion getter pump and a titanium sublimation pump and again the (partial) pressure is monitored via an ion gauge and a residual gas analyzer. The storage rack holds up to 15 samples and two spare tips. On the topmost slot sits a copper block functioning as coolant for annealed samples (crystals are facing down on the sample plate). With a wobble stick, the samples can be transferred between AES/LEIS station, STM station, storage rack, and manipulator.

2.1.2 Omega Laboratory

The system has only one UHV chamber where all sample preparation and analysis procedures take place. A pressure of $\approx 1 \times 10^{-10}$ mbar is maintained by a scroll pump, a turbomolecular pump, an ion getter pump, and periodically pumping with a titanium sublimation pump. The system is equipped with an ion gauge to monitor the pressure and a mass spectrometer for analyzing the residual gas and leak testing.

Samples can be cleaned via sputtering with argon ions and annealing at the heating station. Surface treatment with atomic oxygen or atomic hydrogen is achieved by directing a thermal gas cracker at the sample. Water is dosed by filling the chamber with molecular D_2O at a desired partial pressure for a desired time.

The main analysis technique is STM. XPS and LEIS is provided by an X-ray source, a helium gas can attached to the sputter gun and a hemispherical analyzer. The system is also capable of LEED through a window at the side of the chamber.

Samples can be inserted to or removed from the main chamber via a small vacuum chamber, which is separated from the main chamber by a hand opened valve and pumped by a scroll pump and a turbomolecular pump. Up to eight samples or spare tips can be stored in a sample carousel in the center of the main chamber. A wobble stick is used to transfer samples between the different stages.

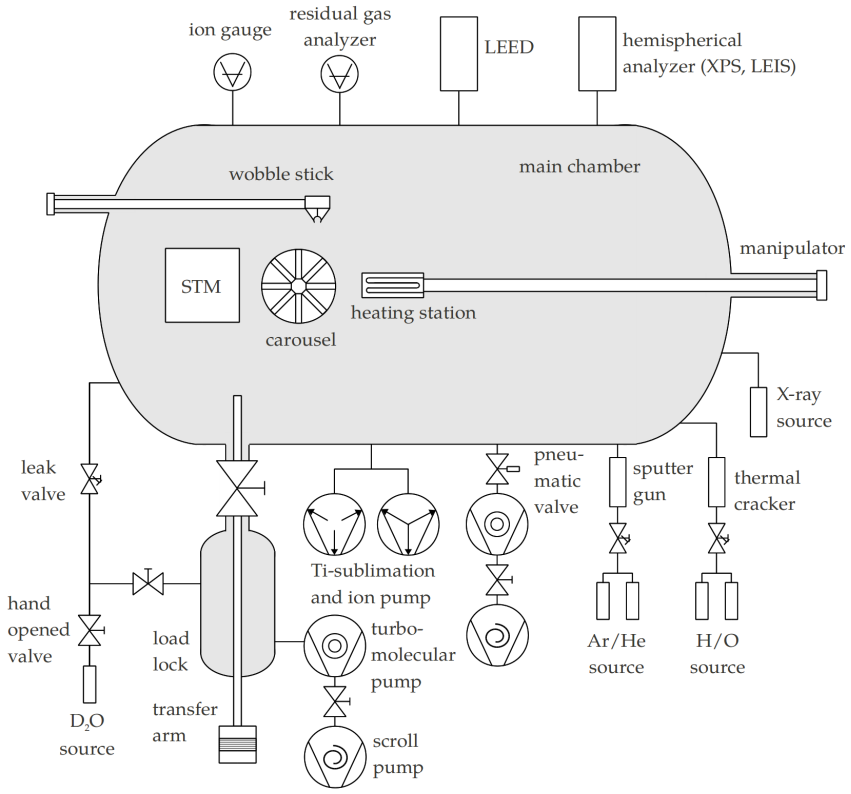

Figure 2.2: *Schematic drawing for the Omega chamber (Figure adapted from reference [31]).*

2.2 Spectroscopy Methods

Several methods for investigation of physical properties were conducted on $In_2O_2(001)$ single crystals. This section gives an overview of the physical principles behind these spectroscopy methods.

2.2.1 Auger Electron Spectroscopy (AES)

Auger Effect When an incident electron with sufficient energy hits a core-shell electron (e.g. a K-electron), the atom gets ionized into an excited state. A bound electron of a higher state (e.g. an L_I-electron) can fill the core hole. The remaining energy can be emitted as a photon with the energy $h\nu(E_K - E_{L_I})$ or it can be transmitted to another electron (e.g. an $L_{II,III}$-electron), which then leaves the atom with the energy

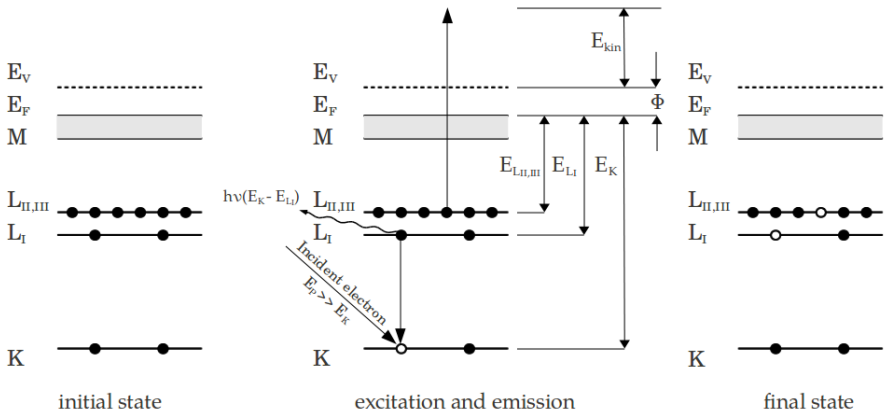

Figure 2.3: *Auger effect: An incident electron ionizes the atom in the 1s (K) level. The core hole is filled by de-excitation of an L_I electron. The remaining energy $E_K - E_{L_I}$ can be emitted as a photon or it can be transferred to another electron - here an $L_{II,III}$ electron - thus further ionizing the atom (Figure adapted from references [30, 32]).*

$$E_{kin} = E_K - (E_{L_I} + E_{L_{II,III}}) - \phi \tag{2.1}$$

where ϕ is the work function. Besides the basic KLL Auger process, also transitions of higher states can happen, resulting in a characteristic spectrum with several peaks for every chemical element. This process of inner ionization is named after Pierre Auger who observed and correctly described the effect in 1923 [33], although it was first discovered by Lise Meitner in 1922 [34].

AES is based on the Auger effect. Inner electrons are removed by an electron beam of 2 - 10 keV directed at the sample and the secondary electrons are collected by a cylindrical mirror analyzer. The emitted Auger electrons have a mean free path of only a few atomic layers, therefore AES is very surface sensitive. Since the Auger energies are characteristic for chemical elements, the count rate of measured electrons per energy bears information about the composition of the sample surface. To reduce the background, typically the first derivative $\frac{dN}{dE}$ of counts over energy is used for analysis to get clear distinctions between the peaks. The difference between minimum and maximum of a signal is called Auger Peak-to-Peak Hight (APPH) and is

often used for comparison of data, although it has to be taken into account that the APPH is strongly dependent on the apparatus and cannot be easily compared to data from different setups.

2.2.2 Hall Measurements

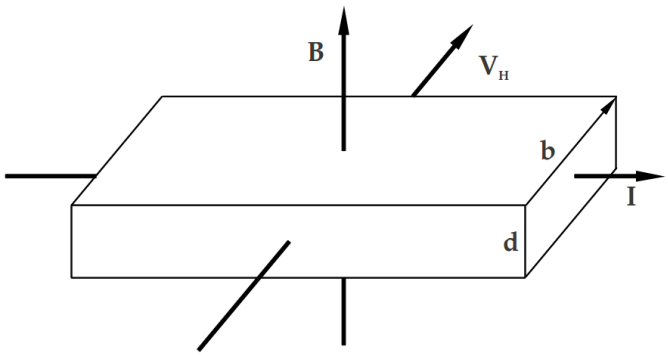

Figure 2.4: *Schematics for the Hall effect (Figure adapted from reference [35]). Current I runs through the sample. An external magnetic field B deflectsts the path of the charge carrieres, leading to the Hall voltage V_H.*

Hall Effect An applied external magnetic field deflects the path of charge carriers in a conductor perpendicular to the field and the direction of current via the Lorentz force

$$\mathbf{F}_L = n \cdot q \cdot (\mathbf{v} \times \mathbf{B}). \tag{2.2}$$

n is the number of charge carriers, q is the charge and $\mathbf{v}$ is the velocity of the charge carriers. The force is compensated by a separation of charge which creates an electrical field $\mathbf{E}_H$ and thus the force $\mathbf{F}_C = n \cdot q \cdot \mathbf{E}_H$ opposite to the magnetic force.

In a rectangular sample with cross section $A = b \cdot d$ this electric field leads to the Hall voltage $V_H = \int \mathbf{E}_H \cdot d\mathbf{s} = \mathbf{b} \cdot \mathbf{E}_H$. Equations

$$q \cdot \mathbf{E}_H = -q \cdot (\mathbf{v} \times \mathbf{B}),$$
$$\mathbf{j} = n \cdot q \cdot \mathbf{v}$$

lead to

$$V_H = -\frac{(\mathbf{j} \times \mathbf{B}) \cdot \mathbf{b}}{n \cdot q}. \tag{2.3}$$

$\mathbf{j} \times \mathbf{B}$ points towards the direction of $\mathbf{b}$, independent whether the current $I = j \cdot b \cdot d$ is carried by positive or negative charged particles. This leads to

$$V_H = -\frac{j \cdot B \cdot b}{n \cdot q} = -\frac{I \cdot B}{n \cdot q \cdot d} \tag{2.4}$$

and

$$V_H = \frac{I \cdot B}{n \cdot e \cdot d} \tag{2.5}$$

for most metals and semiconductors, where the charge carriers are electrons with charge $q = -e$ [35].

Van der Pauw (VdP) Method Arbitrary shaped thin flat samples can be analyzed by the VdP method obtaining the resistivity (2.7) and the Hall coefficients (2.8), which directly lead to the carrier concentration and the carrier mobility. For measurement, the sample must be homogeneous in thickness, must not have holes, and the contacts must be sufficiently small and attached to the edges.

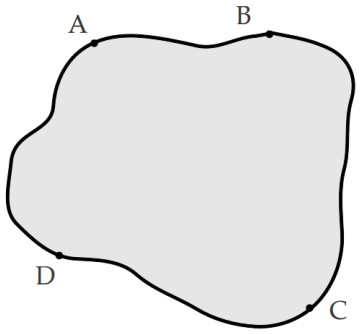

Figure 2.5: *Arbitrary shaped sample for Van der Pauw measurement (Figure adapted from reference [36]). A current is applied through opposed contacts A and C, or B and D, while the resulting voltages between the opposite contacts are observed.*

Four contacts A, B, C, and D are attached to the sample (see figure 2.5). A current is applied between A and B and on the opposite contacts, C and D, voltages are measured, from which the resistivity

$$R_{AB,CD} = \frac{V_C - V_D}{I_{AB}}.$$

can be calculated. Cyclic permutation gives

$$R_{BC,DA} = \frac{V_D - V_A}{I_{BC}},$$

which leads to

$$exp\left(-\frac{\pi d}{\rho} \cdot R_{AB,CD}\right) + exp\left(-\frac{\pi d}{\rho} \cdot R_{BC,DA}\right) = 1, \tag{2.6}$$

where ρ is the specific resistance of the material and d is the thickness of the sample. In general, it is not possible to solve this equation for ρ analytically, but it can be done if the sample has at least one line of symmetry. Then the contacts are attached in that line and from $R_{AB,CD} = R_{BC,DA}$ follows

$$\rho = \frac{\pi d}{ln2} \cdot R_{AB,CD} \cong 4.532 \cdot d \cdot R_{AB,CD}. \tag{2.7}$$

The same setup can be used for measurement of the Hall coefficient. A current is applied between opposite contacts A and C measuring $R_{AC,BD}$. Then a magnetic field is applied perpendicular to the surface leading to the Hall coefficient

$$R_H = \frac{d}{B}\Delta R_{AC,BD}, \tag{2.8}$$

where $\Delta R_{AC,BD}$ is the difference between the resistivities with and without the applied magnetic field. The charge carriers feel the Lorentz force $\mathbf{F} = q \cdot \mathbf{v} \times \mathbf{B}$ perpendicular to the stream lines and perpendicular to the magnetic field. Using $\mathbf{j} = nq\mathbf{v}$, considering only the x-direction and considering the equivalent electric field yields

$$E_H = \frac{1}{nq} j_x B_z = R_H j_x B_z,$$

leading to

$$\frac{1}{nq} = R_H. \tag{2.9}$$

Since q is known, the charge carrier concentration can be obtained [36, 37].

2.2.3 Inductively Coupled Plasma - Mass Spectrometry (ICP-MS)

Inductively Coupled Plasma Argon gas is introduced through a three-cylindrical quartz tube as three separate gas flows. A radio frequency power (usually 27.12 MHz in frequency and 0.5 - 2.5 kW in forward power) is supplied via a coil establishing oscillating electric and magnetic fields. Applying a spark to the argon strips off electrons from the atoms, forming argon ions. These ions are caught in the electromagnetic fields producing further collisions, which lead to the formation of an argon plasma. The plasma consists almost only of single positively charged atoms, so there are almost equal amounts of ions and electrons in each unit of volume. In general the temperature as well as the electron number density in the center of the plasma is lower than in the surrounding, leading to a ring shaped form [38, 39].

ICP-MS For analysis, sample atoms have to be brought into the plasma. Usually this is done by bringing a liquid or dissolved solid sample into a nebulizer or directly gaining an aerosol by using a laser on the sample surface. Once the particles enter the plasma they are completely dissolved into their elements and ionized. The ions are exerted via a series of cones to a mass spectrometer (typically a quadrupole mass analyzer). Information about the chemical composition of the sample can be obtained by analyzing the charge to mass ratio of the measured ions. The plasma preferentially produces positively charged ions, therefore elements that prefer negatively charged configurations like Cl, I, and F are more difficult to measure [39].

2.2.4 Low-Energy Electron Diffraction (LEED)

A beam of electrons with a primary energy ranging from 50 to 300 eV [40] is directed perpendicular to the sample. The de Broglie wavelength

$$\lambda = \frac{h}{p} = \frac{h}{2 \cdot m \cdot E} = \frac{12.3}{(E_{eV})^{\frac{1}{2}}} \mathring{A} \tag{2.10}$$

[41] of these electrons range from 1.7 to 0.7 Å which is just below typical distances between atoms and thus fits for diffraction on the atomic lattice. The electrons are elastically scattered from the surface and observed on a electron-sensitive screen. Since the mean free path of the used electrons is only a few monolayers, LEED is a very surface sensitive analysis method [30].

In application, the electron source is put opposite to the perpendicular sample. The backscattered electrons are visualized on a hemispherical phosphorous screen and collected with a camera. Constructive interference leads to bright spots on the screen, which correspond to the reciprocal lattice.

2.2.5 Low Energy Ion Scattering Spectroscopy (LEIS)

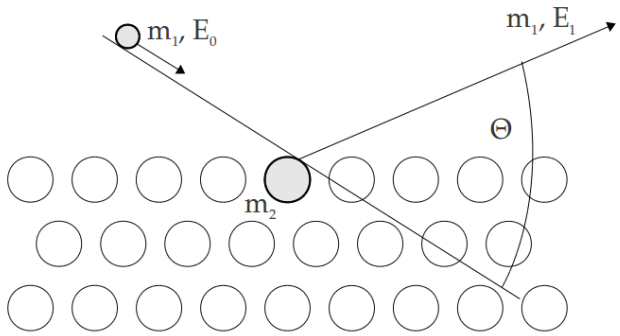

Figure 2.6: *Schematic for an elastically backscattered ion on a solid surface (Figure adapted from references [30]). An impact ion with energy E_0 hits a target atom at rest and is scatterd at the angle Θ with energy E_1.*

Two body scattering An ion with energy E_0 hits the surface of a solid at a given angle and is elastically backscattered by a target atom. The surface atom is considered to be at rest. Lattice oscillations and interaction with neighbor atoms are neglected due to their small influence. Using conservation of energy and conservation of momentum leads to

$$E_1 = E_0 \left(\frac{m_1}{m_1 + m_2} \left(cos\Theta \pm \sqrt{\frac{m_2^2}{m_1^2} - sin^2\Theta} \right) \right)^2 , \tag{2.11}$$

where m_1 is the mass of the impact ion, m_2 the mass of the surface atom, and Θ the angle between the directions of incoming and reflected ion. E_0 gives the starting energy of the ion and E_1 the energy after scattering [30, 32].

LEIS (also known as ISS - Ion Scattering Spectroscopy) An ion beam of defined energy, typically ranging from 100 eV to 10 keV, is directed at the sample at a given angle. Usually helium or neon ions are used because of their low mass and reactivity. Due to the low energy loss via electronic transitions ($\leq 1\%$ of the primary energy [32]) the collisions can be considered as elastic. As shown in equation (2.11), the energy of the backscattered ions, which is measured by a hemispherical analyzer, depends on the initial energy, the masses of the involved atoms and the scattering angle. Therefore, the collected data is characteristic for the masses and hence for the chemical elements on the sample surface. LEIS gives a good qualitative overview of the elements present on surfaces, although it is very difficult to quantify the results due to neutralization of impact ions on the surface. The neutralization probability for 1 keV He^+ ions often lie over 99%, meaning less then one percent of the initial ions can be measured [30]. There is no direct relation between the intensity of the backscattered ion beam and the number of atoms present.

2.2.6 Scanning Tunneling Microscopy (STM)

Quantum Mechanic Tunneling Effect A free particle with kinetic energy E hits a rectangular potential barrier of the energy $V > E$ and width d (figure 2.7). In quantum mechanics, the particle can be treated as a wave function and described by the time independent Schrödinger equation

$$\left(-\frac{\hbar^2}{2m}\Delta + V \right) \psi(x) = E\psi(x). \tag{2.12}$$

This equation can be solved in the three different regions I, II and III resulting in wave functions with wavelengths $\lambda = \frac{2\pi}{|k|}$ for I and III and an exponentially decreasing behavior

$$\psi(x) \propto e^{-\alpha x} \tag{2.13}$$

with

$$k = \sqrt{\frac{2m(V-E)}{\hbar^2}} = i\alpha$$

in region II.

The probability of a particle to be at a specific position is proportional to $|\psi(x)|^2$. The probability of a particle moving through the potential barrier is therefore proportional to $|\psi(d)|^2$ giving the transmission coefficient

$$T \propto e^{-2\alpha d}. \tag{2.14}$$

For a classical particle the transmission would be prohibited, hence the name tunneling effect, which represents the passing of a particle through a potential barrier in the energy diagram [42, 30].

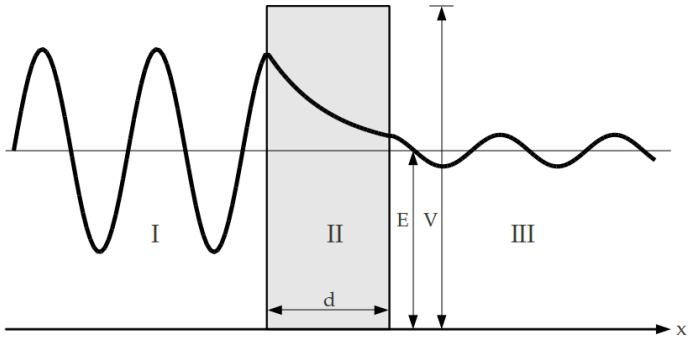

Figure 2.7: *Schematics for a wave function tunneling through an energy barrier (Figure adapted from references [42]). A wave function with the kinetic energy E hits a rectangular energy potential of the energy V, shows an exponentially decreasing behavior in region II, and has a strongly reduced amplitude after the barrier.*

STM A thin tip (typically an electrochemically etched tungsten wire) is moved very close (a few Å) to a conducting sample. Applying a voltage allows electrons to tunnel through the small gap leading to a tunnel current, which is characteristic for the distance between tip and sample (equation (2.14)). Scanning along the surface line by line and collecting recorded data gives a topographic view of the surface on an atomic scale. Since the tunneling current depends on the electronic states on the sample and on the tip, the image does not show actual atoms but their electronic structure within the surface [43, 44].

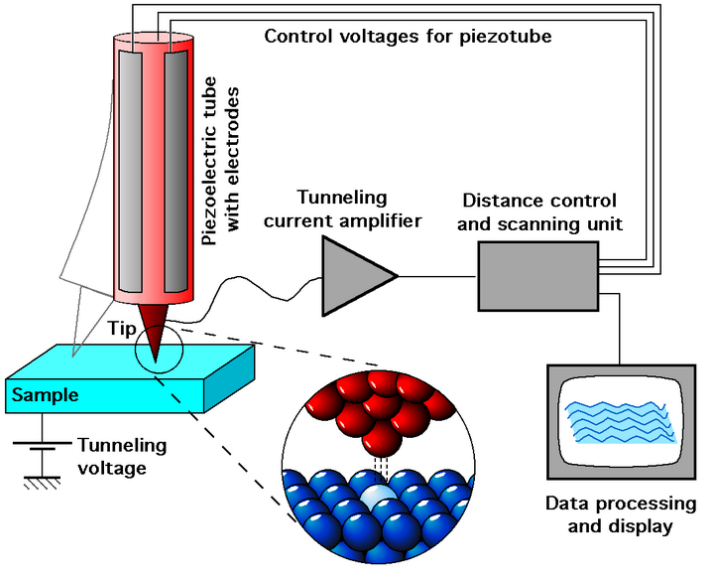

Figure 2.8: *Schematic view of an STM (Figure from reference [30]). An applied voltage between tip and sample leads to tunneling of electrons. The resulting current is amplified and used as a monitor for the distance between tip and sample. The tip is systematically moved along the sample surface and the collected data is assembled to an image of the sample's surface topology.*

Typically STMs are operated in constant current mode, meaning the measuring instruments keep the tip at a constant distance to the sample, permanently approaching and retracting the tip via piezo electronics as it moves along the surface. The changes in height are recorded and linked to the lateral tip position leading to a two dimensional surface profile. Another way of scanning is constant height mode, where the tip's position in z-direction

is fixed and the tunneling current is recorded while lateral tip movement.

In principle STMs work in all isolating surroundings, although they are mainly run in ultra-high vacuum to minimize interaction with the environment.

The first Scanning Tunneling Microscopes were built by Gerd Binnig and Heinrich Rohrer [45, 46] at the IBM research laboratories from 1978 to 1981, which earned them the Nobel prize in 1986.

2.2.7 X-Ray Photoelectron Spectroscopy (XPS)

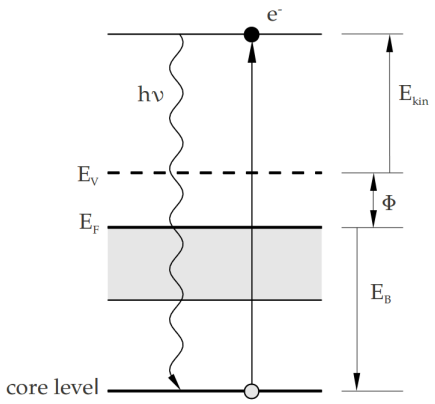

Figure 2.9: *Schematics for the photoelectric effect (Figure adapted from references [30]). A photon hits a core electron with an energy higher than the ionization energy. The electron absorbs the photon and leaves the atom with the energy* $E_{kin} = h\nu - \Phi - E_B$.

Photoelectric Effect Samples that are radiated with photons can emit electrons. The energy of these electrons depend solely on the frequency - and thus the energy - of the impact photons, not on the intensity of the radiation. The number of created photoelectrons is proportional to the intensity. Albert Einstein explained the physical process [47] and received the Nobel price for this work in 1921. Each impact photon is absorbed by exactly one electron. When the received energy $E_f = E_i + h\nu$ is high enough, the electron leaves the surface with the energy

$$E_{kin} = h\nu - \Phi - E_B, \tag{2.15}$$

where ν is the photon frequency, Φ is the work function, and E_B is the binding energy [30, 32, 42].

XPS The sample is radiated with X-rays whose energies are high enough to ionize inner shells. As X-ray source, typically a magnesium or aluminum coated anode is used. Rapidly moving electrons emitted by a filament impinge on the anode at high voltage, causing the emission of X-rays [48]. The energies and the quantity of the emitted electrons are measured in a hemispherical analyzer generating an energy spectrum. The binding energies of inner shell electrons depend on their chemical environment. Therefore, XPS does not only give information about the atoms existing on the surface but also about their chemical states. So XPS is also known as Electron Spectroscopy for Chemical Analysis (ESCA).

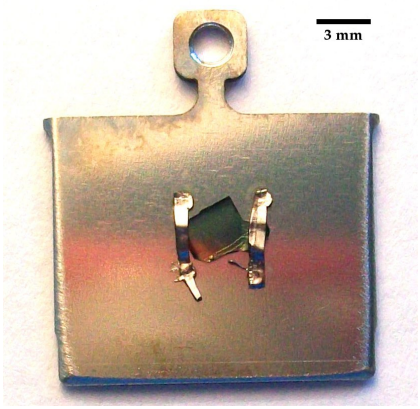

Figure 3.1: *An In_2O_3(001) single crystal from batch 7 mounted on a stainless steel sample plate.*

3 Experimental Results

3.1 Sample Preparation

Sample Mounting The samples are mounted on cleaned stainless steel sample plates with spot welded tantalum strips (see figure 3.1). Before mounting the plates and strips are cleaned with acetone and isopropanol in an ultrasonic bath for ten minutes, and dried with CO_2 snow.

Surface Cleaning The basic preparation in UHV consists of 2-3 cycles of sputtering and annealing. The sputtering cycle consists of 10-15 minutes of bombardment with 2 kV argon ions at an argon pressure of 1.5×10^{-6} mbar resulting in a sputter current of 3.5 μA. Afterwards the sample is kept at 500 °C for 10 minutes. Although a permanent color change above 600 °C [2] in the MgO doped crystal is not observed, temperatures above 500 °C are generally avoided.

Gas Dosing Hydrogen and oxygen from standard gas canisters are split into atomic components using a thermal gas cracker directed at the sample. Typically the gas cracker is operated at 50 W at a gas pressure of 2.5×10^{-7} mbar for 30 minutes and the sample is kept at elevated temperatures of 300 °C or 500 °C. Water is dosed by attaching an evacuated vial containing a drop of D_2O to a leak valve. Water gas is introduced to the chamber by opening

the leak valve between the water source and the chamber until a certain pressure is reached. The sample is then exposed to water for a certain time corresponding to the desired dosage of 1-5 langmuir (where one langmuir corresponds to an exposure of 10−6 torr during one second [49]). Typical parameters for an exposure of two langmuir are 40 s at a D_2O pressure of 5 $\times$ 10^{-8} mbar.

3.2 Auger Electron Spectroscopy

Auger spectra were taken from the samples 2b, 5b, 6b, and 7 to analyze surface terminations and possible differences between the sample compositions. For the untreated samples (measured after inserting to UHV before any cleaning treatments), characteristic peaks for indium and oxygen can be observed and in addition all samples show clear evidence for carbon. The sulfur peak observed by Hagleitner [2] is not found in the samples. There is no data for the MgO doped sample, although no differences to Hagleitner's findings should be expected.

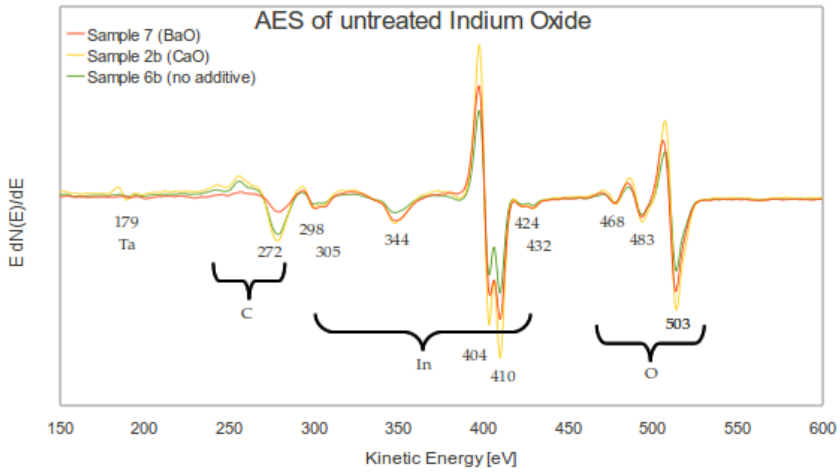

Figure 3.2: *AES of In_2O_3 crystals directly after inserting into UHV, before sample treatment. Reference values taken from reference [50].*

The samples were cleaned several times as described in section 3.1 to remove any impurities from the atmosphere. The final annealing cycle was left out to investigate the surface after sputtering with 2 kV argon ions for 10 minutes. This treatment removed the carbon and sulfur contamination

leaving a small argon peak from the implemented sputter-ions. The small peak at 180 eV is caused by tantalum strips used to fix the sample to the sample plate due to difficult AES focusing for the small sample size.

Spectra taken from the samples after complete preparation (3 cycles of sputtering for 10 minutes with 2 kV argon ions followed by keeping the sample at 500 °C for 10 minutes) show identical results for the different compositions. Neither platinum and lead, nor calcium and magnesium, which are present in the samples in a significant amount (see section 3.4) are observed with AES. Also the differences between oxygen and indium APPH of 53% for MgO additive, 51% for BaO additive, 50% for CaO additive, and 51% for no additive indicate no significant differences between the sample surfaces.

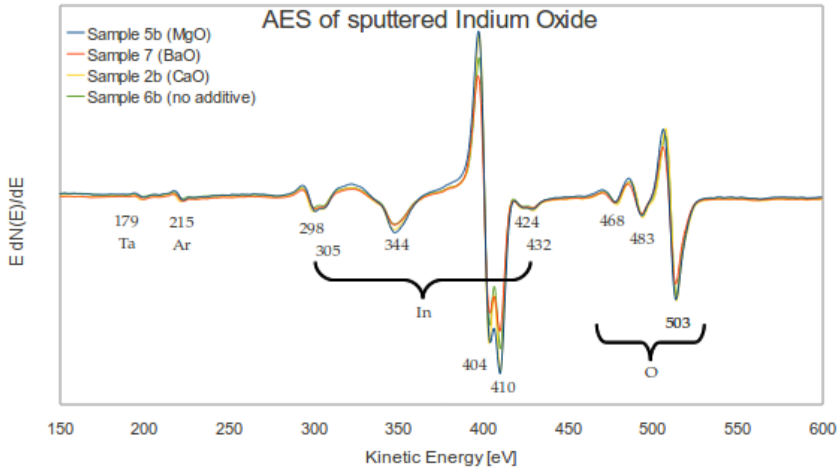

Figure 3.3: *AES of In_2O_3 after two cycles of sputtering and annealing and a third terminating sputtering cycle.*

3.3 Hall Measurements

Hagleitner measured an In_2O_3 from batch 8 by four-point probe method and obtained a resistivity of $\rho = 2 \times 10^5\ \Omega\cdot$ cm. Using the value $\mu = 32\ \mathrm{cm^2 \cdot V^{-1} \cdot s^{-1}}$ for carrier mobility [11] in the relation $n = \frac{\sigma}{e \cdot \mu}$ for carrier concentration [51] leads to the value $n = 1 \times 10^{12}\ \mathrm{cm^{-3}}$ [1], which is seven orders of magnitude lower than values reported in literature before [11].

Since the four-point probe method is not very accurate, Patrick Heinrich, Institute of Solid State Physics, Vienna University of Technology, conducted

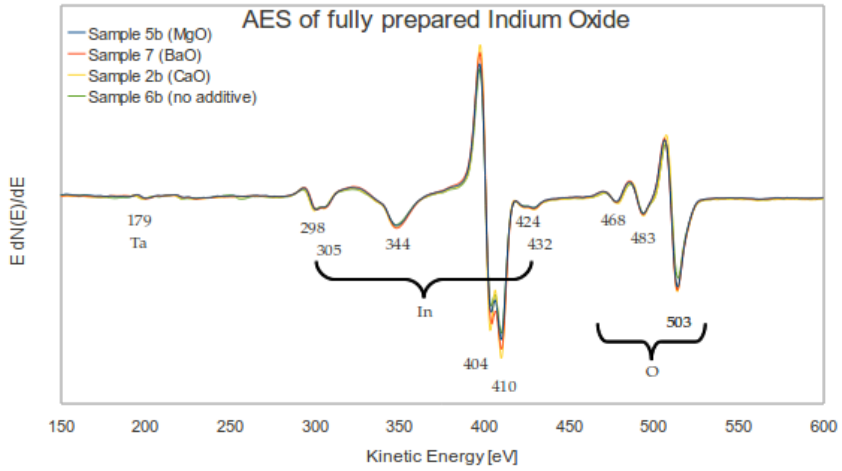

Figure 3.4: *AES of In_2O_3 after 3 cycles of sputtering and annealing.*

Hall measurements on samples 2a, 5d and 8. The results (shown in table 3.1) for samples 2a and 5d are in the order of magnitude of previous measurementes [25]. For sample 8 a carrier concentration of $\approx 3 \times 10^{14}$ cm^{-3} is found. This value cannot completely be trusted because the setup is not optimized for almost insulating samples, but it confirms values for carrier concentrations and carrier mobilities much lower than observed on any other indium oxide crystals.

#	additive	Mol %	n [cm^{-3}]	ρ [Ω·cm]	μ [cm^2/V·s]
2a	CaO	1.5	7.03895×10^{18}	0.024789	35.77
5d	MgO	1.5	6.07388×10^{17}	1.4165	9.7
8	?	?	3.38687×10^{14}	1.044×10^5	0.1765

Table 3.1: Results for Hall measurements on samples 2a, 5d, and 8.

This results prove again the uniqueness of In_2O_3 crystals from batch 8 and although he tried many different growing conditions, Boatner has not yet found the exact parameters for crystals similar to samples 8.

3.4 Inductively Coupled Plasma - Mass Spectrometry

ICP-MS measurements were conducted by Andreas Limbeck, Institute of Chemical Technologies and Analytics, Vienna University of Technology. As

mentioned in section 1.2, the flux for sample growing consists of B_2O_3 and PbO with additional MgO, CaO, or BaO. Therefore, in addition to the main composition of indium and oxygen, traces of B, Mg, Ca, Ba, and Pb are expected (detailed description for the fluxes of the different samples are listed in table A.1). The results (table 3.2) show that boron and barium are hardly present in the sample, while lead and platinum (coming from the crucible) are present in significant amounts. When added, magnesium and calcium are found in the sample, although especially for magnesium there seems to be no direct relation between the ratio of added Mg and the amount present in the sample. It needs to be mentioned that ICP-MS has difficulties measuring Ca, because the main isotope is overshadowed by argon atoms of the same mass present in the plasma.

The results also helped to compare the samples used in this thesis to the crystals Hagleitner analyzed [1, 2]. Unclear are the significantly higher concentrations of Mg, Pt, and Pb in sample 5b, the crystal mainly investigated in this thesis, which should be almost identical to sample 5d according to the growing environment.

			elements (ppm)					
#	**additive**	**Mol %**	**B**	**Mg**	**Ca**	**Ba**	**Pt**	**Pb**
1	CaO	2.75	3	1	251	0	3607	5956
2a	CaO	1.5	4	4	112	0	1753	1726
2b	CaO	1.5	1	0	24	0	47	358
3	MgO	2.75	3	881	1	0	1291	3928
4a	MgO	2.5	2	1849	22	0	2366	10270
4b	MgO	2.5	1	1908	7	0	3378	11185
5a	MgO	1.5	3	241	1	0	476	1119
5b	MgO	1.5	1	2307	2	0	3963	15233
5c	MgO	1.5	5	220	0	0	53	413
5d	MgO	1.5	1	363	2	0	117	1262
6a	-	-	2	0	10	0	3911	8166
6b	-	-	1	0	3	0	84	362
7	BaO	1.5	2	0	2	1	3213	6066
8	?	?	0	1388		0	155	4307

Table 3.2: Results for ICP-MS measurements, including the results for the crystal used by Hagleitner [1]. See figure 1.1 for photos of the crystals used for ICP-MS.

3.5 Low-Energy Electron Diffraction

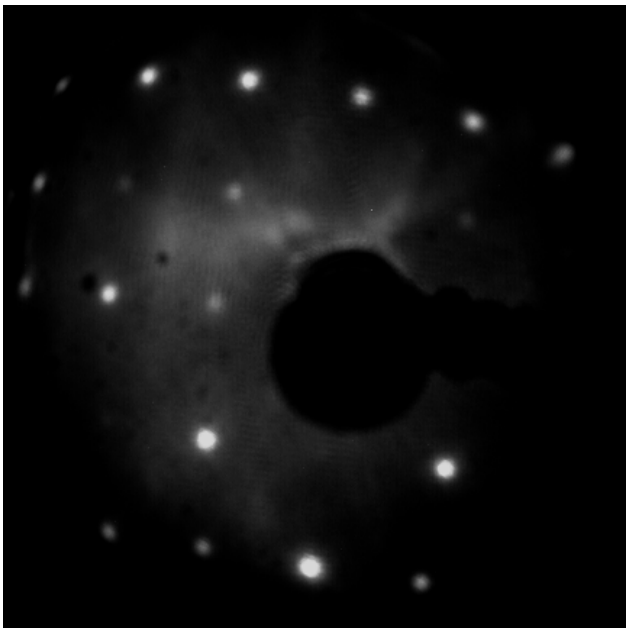

Figure 3.5: *LEED patterns for the reduced In_2O_3 (001) surface ($E_{electron}$ = 60 eV).*

According to calculations, the $In_2O_3(001)$ surface is only stable at strongly reducing conditions. In more oxidizing environment, faceting, especially into (011) and (111) surfaces, is expected [8]. An easy way to observe surface faceting effects is comparing LEED patterns in respect to changing the energy of the primary electrons. Slight variations of electron energy should lead to significant fluctuations in the LEED images (see figure 3.6).

The following LEED images can only be considered qualitatively because of their poor quality due to the experimental setup (The LEED screen could not be brought close enough to the sample, because it was blocked by the installed thermal cracker.). Figure 3.5 shows the LEED pattern of the cleaned sample, which is in agreement to earlier LEED studies [2, 52]. Figures 3.7 and 3.8 compare LEED images of oxidized and water dosed crystals at different electron energies. No significant changes occur in the LEED patterns, ruling out faceting of the surface.

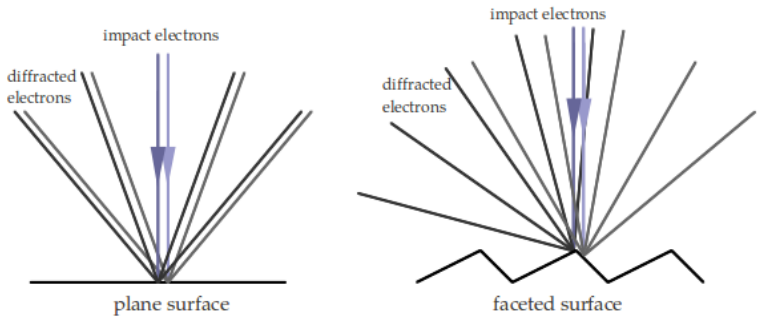

Figure 3.6: *Schematic for LEED on a plane and on a faceted surface. The angle between diffracted electrons depends on their impact energy. LEED on a faceted surface shows more (and less sharp) LEED spots due to the zig-zag pattern and energy variations of the impact electrons leads to bigger variations of the LEED patterns.*

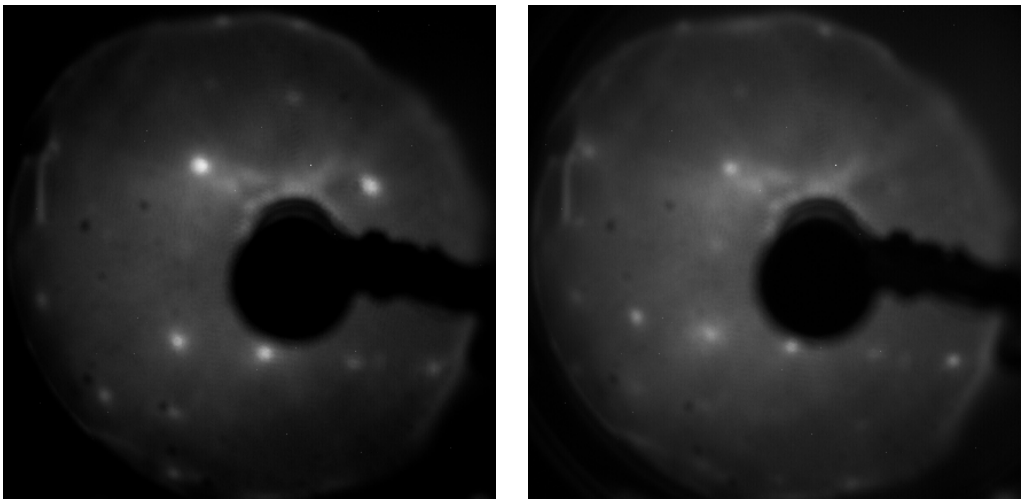

Figure 3.7: *A comparison of LEED images of the oxidized surface at* $E_{electron}$ *= 80 eV (left) and* $E_{electron}$ *= 90 eV (right).*

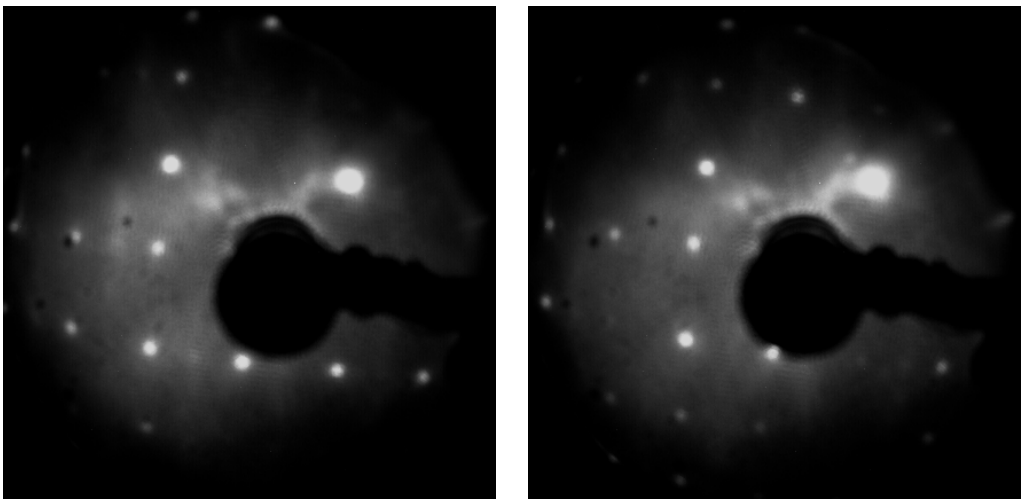

Figure 3.8: *A comparison of LEED images of the water dosed surface at $E_{electron}$ = 60 eV (left) and $E_{electron}$ = 70 eV (right).*

3.6 Low Energy Ion Scattering Spectroscopy

3.6.1 LEIS Comparison of Different Crystals

Low Energy Ion Scattering spectra on the samples 2b, 5b, 6b, and 7 show the same results as AES for surface termination and are in perfect agreement with previous results [2]. The oxygen peak (at about 595 eV) and the indium peak (at about 932 eV) are clearly seen on all of the samples. The higher count rate for indium compared to oxygen confirms the expected metallic surface termination. The small shoulder on sample 6b is caused by chromium from the stainless steel sample plate.

3.6.2 LEIS Comparison after Different Surface Treatments

LEIS measurements were performed on crystal 5b for sputtered and annealed, oxidized, and water dosed surfaces. A clear increase of the oxygen peak in respect to the indium peak can be observed due to a change from indium to oxygen surface termination.

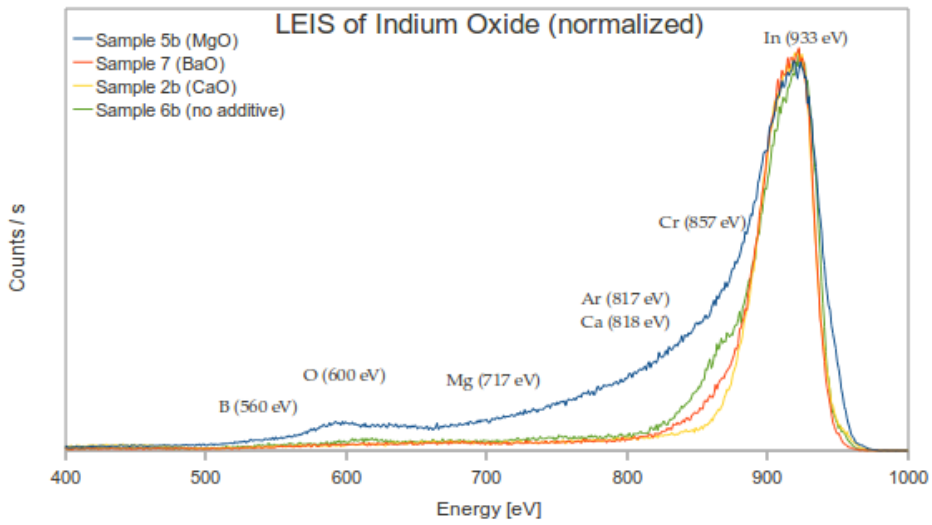

Figure 3.9: *A comparison of LEIS spectra of differently doped samples after full preparation. Scattering angle: 90 °; E_{He^+}: 1000 eV; $I_{Emission}$: 4.8 mA; p_{helium}: 9 × 10^{-8} mbar; I_{target}: 55 nA, 5 repetitions. Sample 5b is the reference spectrum, sample 7 is normalized by a factor of 1.67, sample 2b by a factor of 1.57, and sample 6b by a factor of 2. All relevant elements are listet: elements present in the sample (see table 3.2), argon from the sputter cycle, chromium from the sample plate, and tantalum from the sample mounting.*

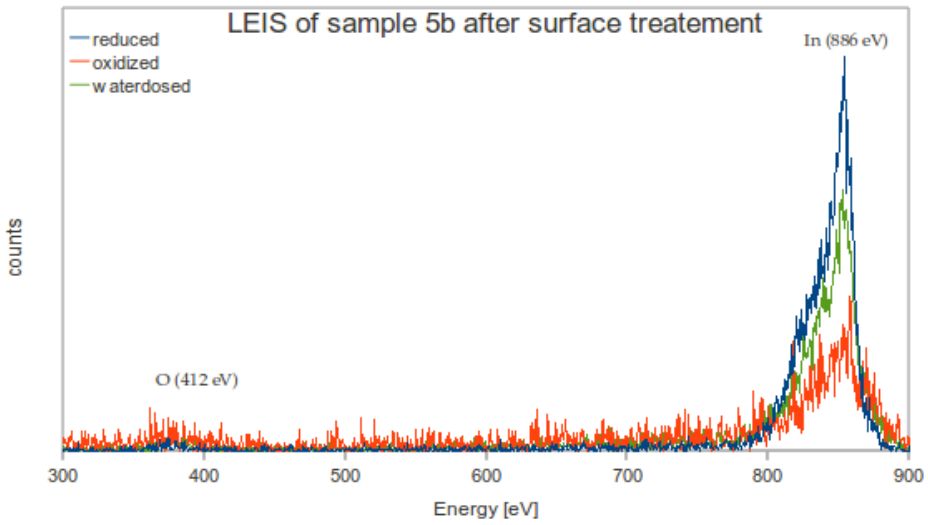

Figure 3.10: *A comparison of LEIS spectra of differently treated MgO doped sample 5b. Scattering angle: 137 °; E_{He^+}: 1000 eV; $I_{Emission}$: 5 mA; p_{helium}: 5 × 10^{-8} mbar; I_{target}: 75 nA. The sample was reduced by three cycles of sputtering for 15 minutes with argon ions and annealing at 500 °C for 10 minutes. Oxydizing was done by bombarding the surface with O-atoms for 30 minutes at an oxygen pressure of 2.5 × 10^{-8} mbar, while keeping the crystal at 500 °C. Water was dosed by exposing the sample to a D_2O pressure of 5 × 10^{-8} mbar for 100 s resulting in a dosage of 5 langmuir.*

3.7 Scanning Tunneling Microscopy

3.7.1 Comparison of Differently Doped Crystals

Scanning tunneling microscopy was used to compare the surface structure from samples grown with different flux additives. Again samples 2b, 5b, 6b, and 7 with dopants of CaO, Mgo, Bao, or no dopants were investigated. Although all crystals share basic surface features, there are significant differences between the compositions (see figures 3.11 and 3.11). On all samples only steps of 5 Å can be seen. The BaO and MgO doped samples show large terraces, while CaO and undoped samples have many step edges and small terraces. The topmost layer is not fully covered and consists of atomic clusters sitting on a 2.5 Å deeper lying 3.6 Å square lattice (it is very difficult to obtain atomic resolution, especially between the topmost clusters, but at least on the MgO doped sample, the 3.6 Å lattice can clearly be seen in the Fourier transform). Again BaO and MgO doped samples differ from the CaO and undoped samples in ordering of the topmost layer. The former tend to have rows of 2 atoms separated by rows of a missing atoms, while the latter form zigzag shaped surface atom ordering. Apart from image quality, changing tunnel voltages has no effect on the results.

The large circular elevations of the surface (clearly seen in figure 3.11 a) and c)) are likely argon bubbles arising from argon ions implanted during the sputtering cycle of the surface cleaning process.

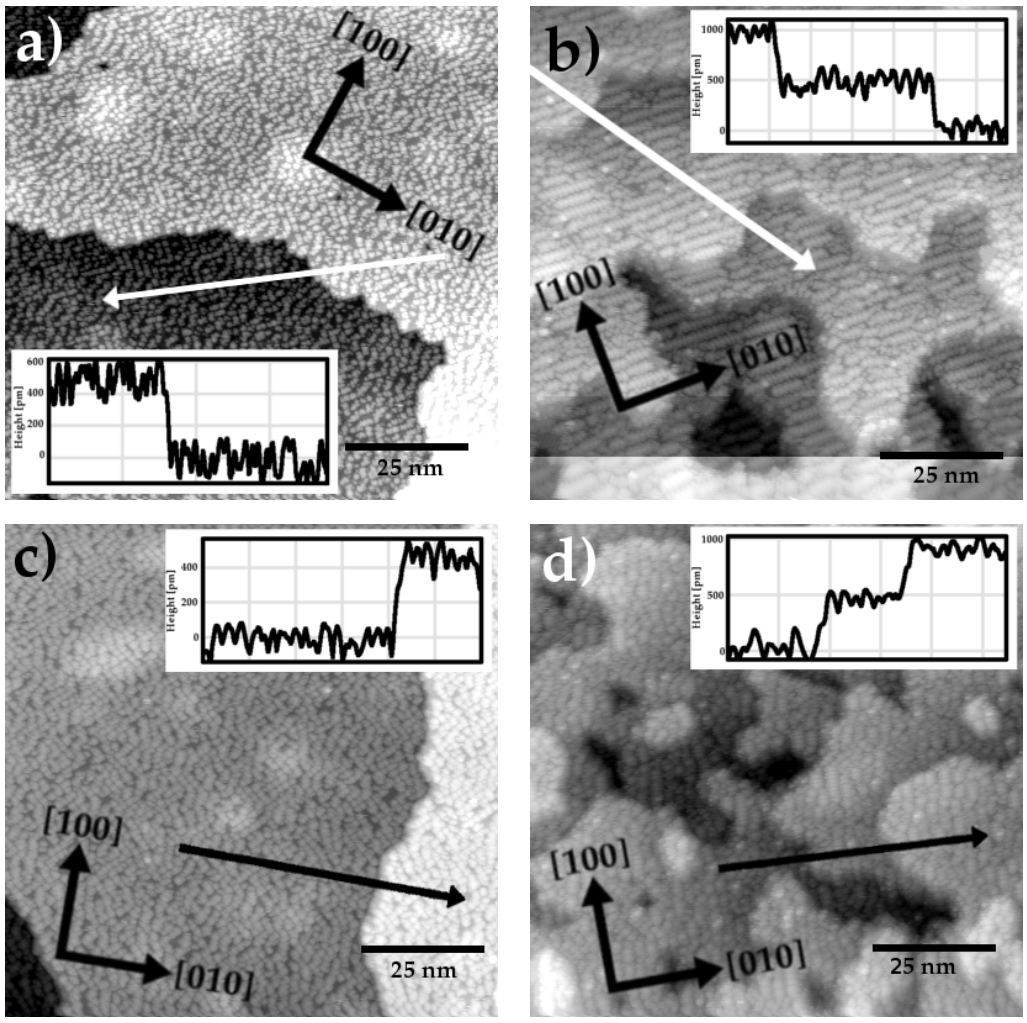

Figure 3.11: *These STM images show 100 × 100 nm² scans taken with the RT STM. a) Sample 7, BaO (image #1008), Gap Voltage: +1.71 V Feedback Set: 0.47 nA; b) Sample 2b, CaO (image #1216), Gap Voltage: -2.23 V Feedback Set: 0.52 nA; c) Sample 5b, MgO (image #1015), Gap Voltage: -3.08 V Feedback Set: 0.44 nA; d) Sample 6b, no additive (image #1103), Gap Voltage: -2.32 V Feedback Set: 0.52 nA*

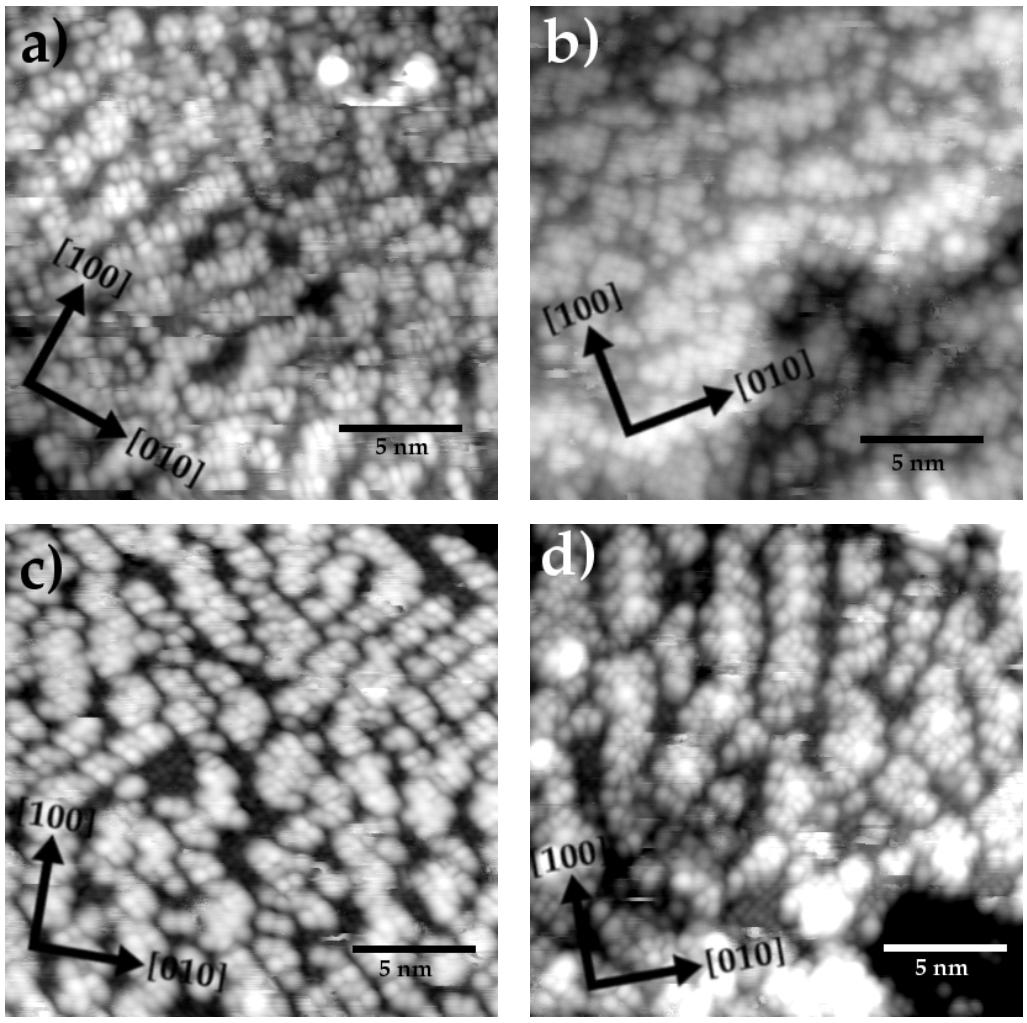

Figure 3.12: *These STM images show 20 × 20 nm^2 scans taken with the RT STM. a) Sample 7, BaO (image #1032), Gap Voltage: -1.71 V Feedback Set: 0.52 nA; b) Sample 2b, CaO (image #1120), Gap Voltage: -2.52 V Feedback Set: 0.50 nA; c) Sample 5b, MgO (image #1084), Gap Voltage: -2.05 V Feedback Set: 0.46 nA; d) Sample 6b, no additive (image #1020), Gap Voltage: -1.97 V Feedback Set: 0.52 nA*

3.7.2 Analysis of MgO Doped Crystals

A sample from batch 5b (1.5 Mol % MgO additive) was thoroughly investigated in the Omega chamber. Scans for the reduced (sputtered and annealed) surface lead to similar results as shown in previous investigations [1]. Both, scanning with positive and negative voltage is possible, although negative voltage lead to better resolution. Ideal scanning parameters vary around a gap voltage of -3 V and a feedback set of 0.25 nA. Large scale scans show large terraces with step edges of 5 Å height. Patterns of protrusions on a 2.5 Å deeper lying plane are observed. These protrusions align along rows and columns of pairs of atoms. The patterns can be reproduced easily by equivalent surface preparation and are consistent with images taken in the RT STM and previous work [1]. Closeup scans of the surface (figure 3.14) show atomic resolution beneath the protrusions. Fast Fourier transform analysis reveals a regular 3.6 Å square lattice in [110] direction. A close look at the images show that not every lattice site has the same brightness and every second lattice site in every second column remains black (see figure 3.13). The protrusions above this lattice sit close by sites of the same lattice but are distorted in respect to the regular lattice beneath.

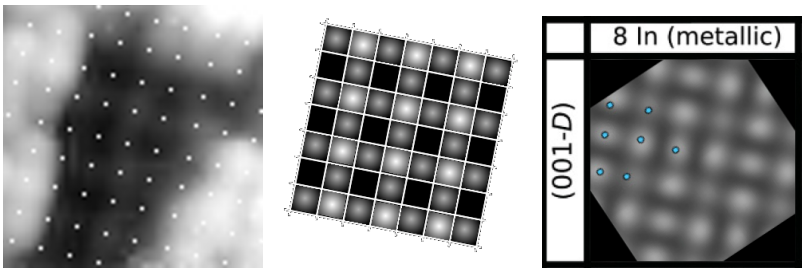

Figure 3.13: *A comparison of the sublattice measured by STM (image #1837) on the left and a simulated STM image [8] on the right side, respectively. The figure in the middle shows a schematic drawing of the experimental data. The dark sites possibly correspond to the less bright sites in the simulated image, this resemblance possibly indicates that the sublattice could be a D-layer.*

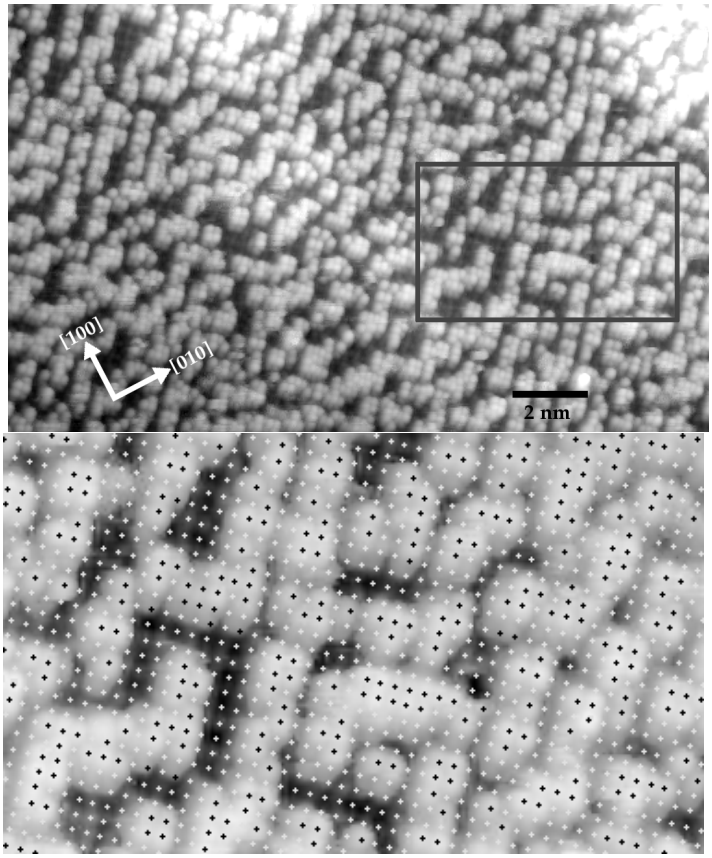

Figure 3.14: *An STM image taken with in the Omega chamber. Clean surface (image #1837), Gap Voltage: -3.10 V Feedback Set: 0.26 nA. The 3.6 Å lattice can clearly be seen.*

3.7.3 Influence of Hydrogen, Oxygen and Water on the Surface

The crystal was exposed to atomic oxygen, atomic hydrogen (directing a gas cracker at the sample for about 30 minutes, mostly keeping the sample at elevated temperatures), and water (filling the chamber to defined pressures of D_2O, resulting in a surface exposure of a few langmuir).

Oxidizing at room temperature leads to a rough surface. Basic surface features remain the same (large terraces and 5 Å step edges, protrusions on a 2.5 Å deeper-lying layer) but the typical rows and columns of the reduced surface disappear. Oxidizing at 300 °C (figures 3.15 b) and 3.16 b)) increases the surface roughness. Step edges can still be seen, but their heights are difficult to read out of line profiles. Increasing temperatures to 500 °C while oxidizing leads to further roughness. The surface gets more difficult to scan and atomic resolution is impossible to obtain.

The effect of atomic hydrogen is much less severe. Terrace steps remain clearly recognizable and although distorted, patterns similar to the rows and columns of the reduced sample can be observed (figures 3.15 c) and 3.16 c)). Single bright features appear throughout the surface. According to Agoston and Albe [8], forming of hydroxyls on the surface should be the most stable state. Complete coverage was not observed but the single features indicate hydroxyls on the surface. The features disappear after heating the sample to 300 °C or more which is consistent with simulations [8] supporting their interpretation as surface hydroxyls.

Similar results were achieved by exposing the crystal to water. The basic structure of the reduced sample was not altered, but hydroxyls appeared (figures 3.15 d) and 3.16 d)). The sample was dosed with 1, 2 and 5 langmuir with no obvious change in the number of surface features. Also scanning a reduced sample after leaving it in the chamber over night showed similar surfaces which is not surprising since regarding a water background pressure of 10^{-10} mbar, the exposure sums up to a few langmuir after a day.

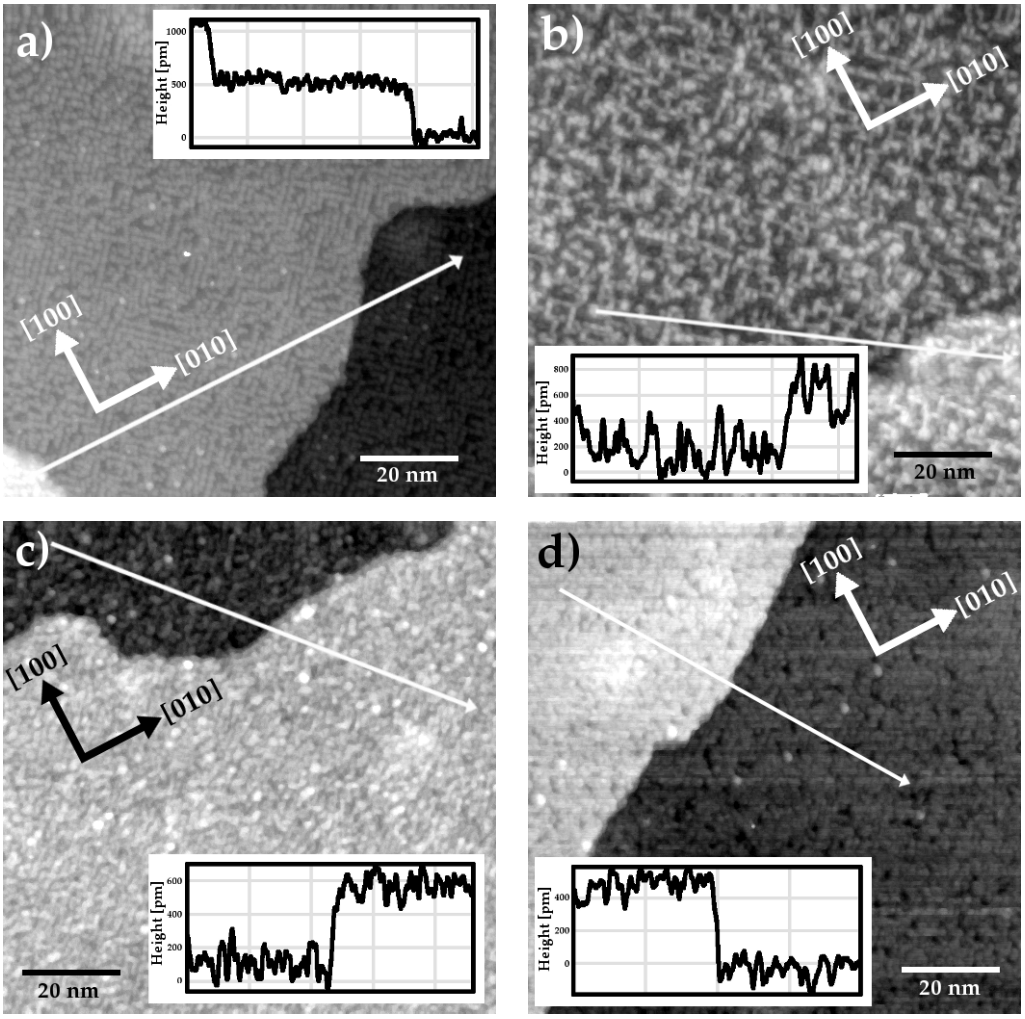

Figure 3.15: *These STM images show 100 × 100 nm^2 scans taken with the Omega STM. a) Reduced surface (image #1075), Gap Voltage: +2.48 V Feedback Set: 0.25 nA; b) Oxidized surface (image #1157), Gap Voltage: +2.50 V Feedback Set: 0.26 nA; c) Hydrogenated surface (image #1873), Gap Voltage: -2.80 V Feedback Set: 0.25 nA; d) Water dosed surface (image #2067), Gap Voltage: -4.00 V Feedback Set: 0.25 nA*

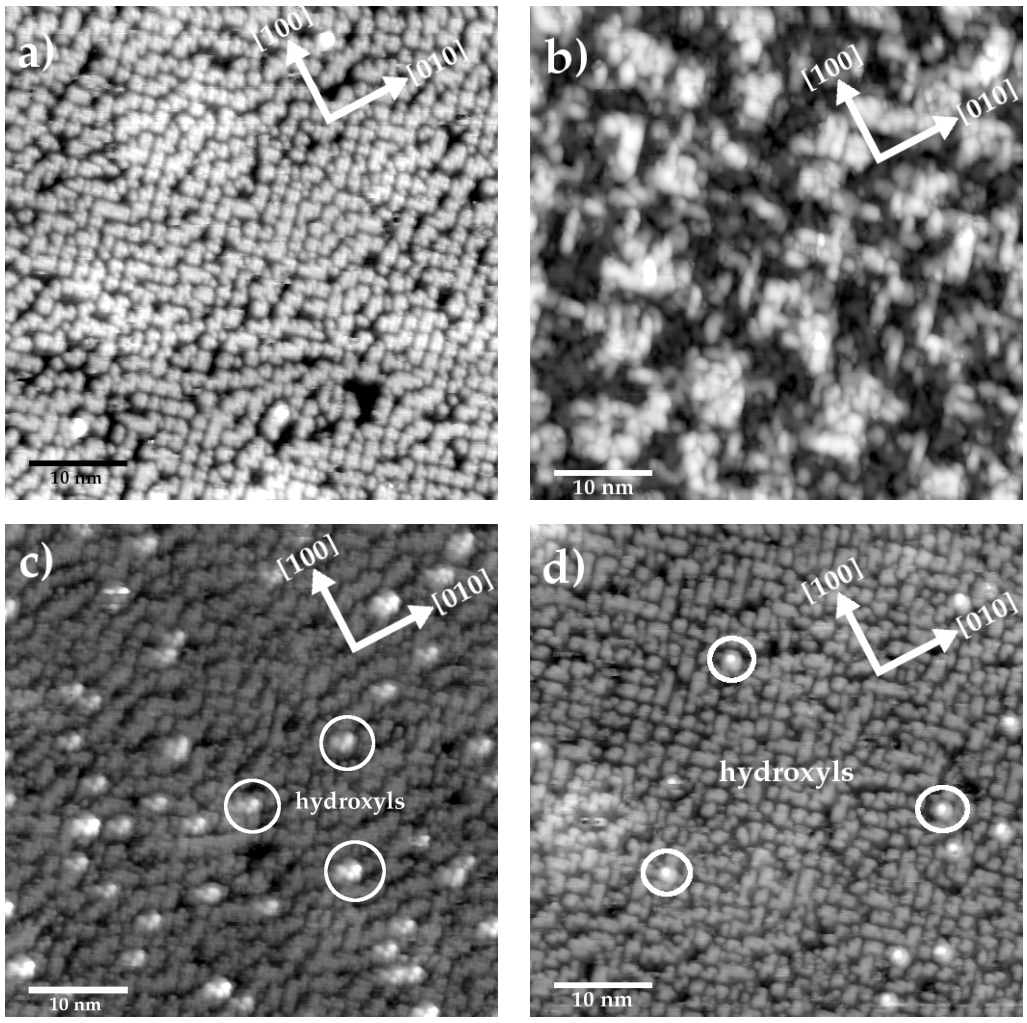

Figure 3.16: *These STM images show 50 × 50 nm^2 scans taken with the Omega STM. a) Reduced surface (image #1740), Gap Voltage: -3.00 V Feedback Set: 0.30 nA; b) Oxidized surface (image #1133), Gap Voltage: +1.60 V Feedback Set: 0.30 nA; c) Hydrogenated surface (image #1758), Gap Voltage: -2.60 V Feedback Set: 0.30 nA; d) Water dosed surface (image #1954), Gap Voltage: -3.75 V Feedback Set: 0.25 nA*

3.8 X-Ray Photoelectron Spectroscopy

XPS was performed after different surface treatments using Mg Kα X-rays ($\approx$ 1253.6 eV). The spectra show a clean surface with clear indium and oxygen peaks. There is no immanent effect after surface treatment with oxygen, hydrogen, or D_2O (see figure 3.17). Looking into detail, the O 1s peak slightly increases in respect to the In 3d peak after oxidizing the crystal, indicating an increase of surface oxygen. No hydroxyls or band bending (as reported by Hagleitner using PES [1]) were observed (see figure 3.18) which is believed to be caused by the limited energy resolution of the instrument.

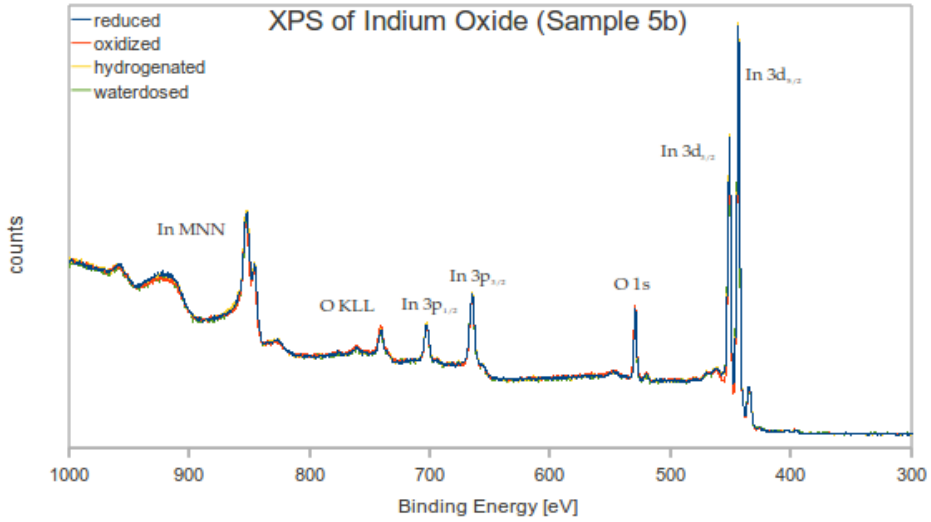

Figure 3.17: *Comparison of XPS spectra for reduced, oxidized, hydrogenated, and water dosed $In_2O_3(001)$. The sample was reduced by three cycles of sputtering for 15 minutes with argon ions and annealing at 500 °C for 10 minutes. Oxydizing and hydrogenating was done by bombarding the surface with O- or H-atoms for 30 minutes at an oxygen or hydrogen pressure of 2.5×10^{-8} mbar (for oxygen, the sample was kept at 500 °C). Water was dosed by exposing the sample to a D_2O pressure of 5×10^{-8} mbar for 100 s resulting in a dosage of 5 langmuir.*

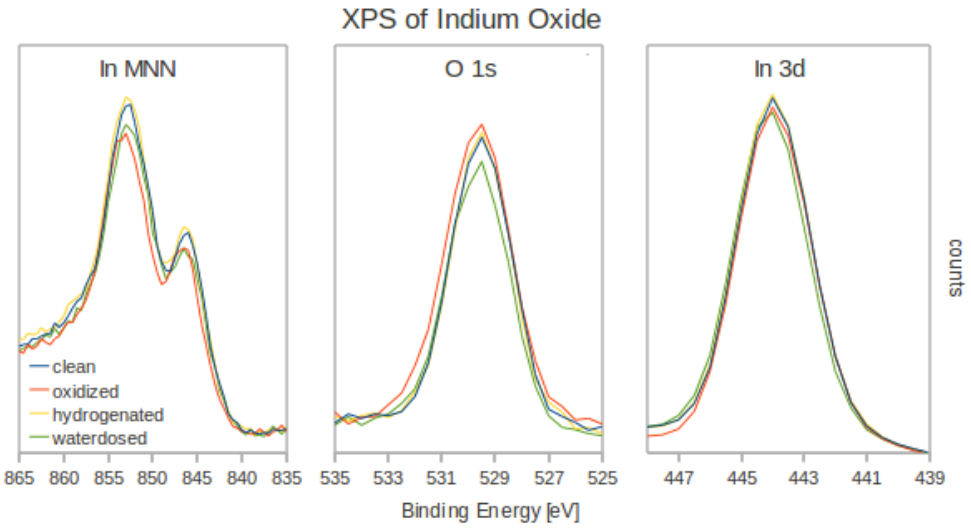

Figure 3.18: *A close up for the indium Auger, oxygen 1s and indium 3d XPS peaks for reduced, oxidized, hydrogenated, and water dosed* $In_2O_3(001)$.

4 Discussion

4.1 Comparison of Different Sample Compositions

4.1.1 ICP-MS

With Inductively Coupled Plasma Mass Spectrometry we had access to a powerful tool for analyzing the exact composition of our samples. It turns out that the major part of impurities is caused by lead from the flux and platinum from the crucible. Residual boron, barium, and calcium can be neglected (although the results for calcium need to be taken with care because of the difficult Ca detection with ICP-MS). Magnesium, however, seems to play a crucial role for sample properties. Only samples with MgO present in the flux show good transparency (samples 3, 4 and 5 in figure 1.1) and also the sample investigated by Hagleitner [1, 2], whose exact growing conditions remain unknown, contain considerable amounts of magnesium. Reproducing identical samples is not trivial. Although grown in fluxes with equal proportions of substrates, the color of the resulting crystals and ICP-MS results show clear differences between the batches.

4.1.2 Electric Conductivity

According to literature [25], In_2O_3 has carrier concentrations of $n = 2 \times 10^{19}$ cm^{-3} and resistivities ranging from 10^{-4} Ω·m to 5×10^{-6} Ω·m [29]. Four-point probe measurements on a crystal from batch 8 revealed a resistivity of $\rho = 2 \times 10^5$ $\Omega\cdot$ cm [1]. Hagleitner concluded a carrier concentration of $n = 1 \times 10^{12}$ cm^{-3} using a value for the carrier mobility found in literature.

Since the four-point probe method is not very accurate and the assumption for the carrier mobility to be the same in a sample that differs in many respects from samples analyzed in previous publications, further investigation was needed. Hall measurements were conducted which were able to both, reveal the resistivity and the mobility at the same time leading to more reliable values for the charge carrier concentration.

The Hall setup was not optimized for measuring almost insulating samples as expected from Hagleitner's sample. So the extremely low carrier concentration of $n = 1 \times 10^{12}$ cm^{-3} was not found, but the measured mobility of ≈ 0.2 $cm^2 \cdot V^{-1} \cdot s^{-1}$ reveals the value $n \approx 3 \times 10^{14}$ cm^{-3} which lies at least three orders of magnitude below values found in previous investigations. It is astounding that the carrier concentrations for both CaO and MgO fluxes

lie in the ranges of previous works. At least the MgO doped sample was expected to have comparable physical properties to crystals of batch 8, since according to STM and ICP-MS investigations, they have a similar composition. This finding leads to the conclusion that little differences in crystal impurities have a big influence on their physical properties.

4.1.3 Surface Structure

LEIS and AES measurements of sputtered and annealed samples confirm $In_2O_3(001)$ surfaces with indium termination and no impurities. The STM images show consistent step edges of 5 Å and protrusions on 2.5 Å deeper lying layer for all compositions. This concludes in a preferred surface with indium termination of only one kind (M- or D-layer) under reducing conditions as already found by Hagleitner [1] and predicted by Agoston and Albe [8].

Remarkable are the surface differences of the samples. The scale of the terraces and the order of the protrusions depend on the crystal compositions. The BaO and MgO doped samples resemble each other more than the CaO and undoped crystals, which have features in common. Taking the ICP-MS results into account, there are only three elements present in considerable amount that could be responsible for the differences. Magnesium can be neglected, because it is only present in one of the four samples, leaving platinum and lead as critical elements.

		elements (ppm)		
#	**additive**	**Mg**	**Pt**	**Pb**
2b	CaO	0	47	358
5b	MgO	2307	3963	15233
6b	-	0	84	362
7	BaO	0	3213	6066
8	?	1388	155	4307

Table 4.1: Results for ICP-MS measurements.

The analyzed crystals with BaO and MgO additives have a high amount of Pt and Pb impurities, whereas the crystals with CaO and without additive have low amounts of Pt and Pb. Taking Hagleitner's crystal into account (sample 8), which has a low amount of Pt and a high amount of Pb, leads to the conclusion that either the presence of lead or the absence of platinum is responsible for the particular surface stoichiometry.

4.2 Surface Structure of MgO Doped $In_2O_3(001)$

4.2.1 Reduced Surface

Metallic termination of $In_2O_3(001)$ in reducing environment [1, 8] was confirmed. The presence of solely 5 Å step edges means that the surface consists only of one particular termination, either M or D. The images with atomic resolution in the sublattice show a regular 3.6 Å lattice in [110] direction, where every second lattice site in every second column remains dark. Both M- and D-layer consist of a 3.6 Å lattice in [110] direction (see figure 4.1). The blank sites could correspond to the less bright atoms of the simulated STM images in figure 3.13, which suggests that the sublattice is a D-layer.

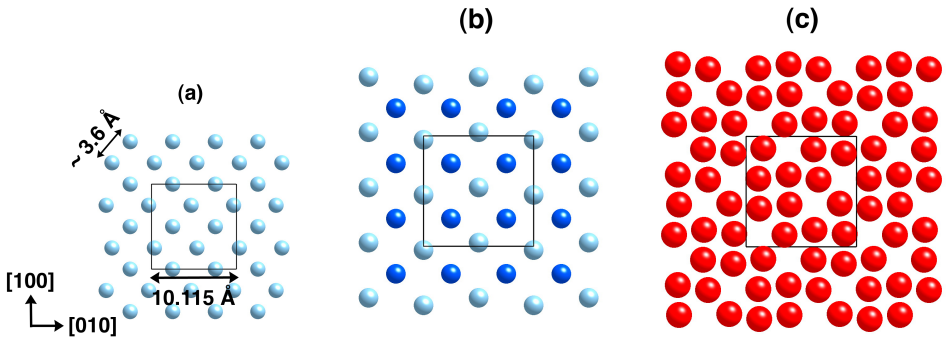

Figure 4.1: *Crystal model for bulk layers of a (a) D-layer, (b) M-layer, and (c) O-layer of the $In_2O_3(001)$ surface (Figure from reference [1]). Note that for stoichiometric surfaces half the atoms are expected to be missing due to surface polarity.*

The protrusions on top of the D-layer would then be expected to be a half-filled M-layer which cannot be the case for two reasons: Counting the number of protrusions leads to approximately two per unit cell corresponding to 1/4 of the lattice sites, which is only half of the expected value. The second reason are the lattice sites occupied by atoms. The M-layer is a distorted 3.6 Å lattice with sites sitting between the D-layer sites, but the atoms observed by STM sit near the same lattice sites as the structure beneath.

4.2.2 Oxygen, Hydrogen, and Water on the Surface

Faceting into energetically preferred surfaces (111), (011), and (211) was ruled out by LEED studies. According to Agoston and Albe [8], in oxidizing environment the $In_2O_3(001)$ surface should consist of a half filled oxygen layer with an In-D layer below. In strongly oxidizing environment, which is the case for the investigations in this thesis, a formation of dimers on the surface is expected.

An increase of surface oxygen is observed by LEIS, although the indium peak remains dominating. STM images show less uniform surfaces, where the disorder is even larger if the oxygen was dosed at elevated temperatures. The high roughness of the surface makes it impossible to obtain atomic resolution and to prove or disprove a consistent oxygen termination. The images taken indicate that an oxidized $In_2O_3(001)$ surface shows no simple dimerized surface as suggested by Agoston and Albe [8], and further investigation is necessary.

Neither dosing hydrogen as atomic H nor in the form of D_2O leads to fully hydroxylated surfaces as shown in figure 1.7. XPS shows no shoulders on the higher energy side of the O 1s peak as would be expected of water or OH on the surface [53]. The occurring single features allocated throughout the surface can be interpreted as hydroxyls, which should appear bright in STM according to simulations [8]. Heating the hydrogenated sample to at least 300 °C leads to a removal of the bright atoms, which is also consistent with calculations [8]. A complete coverage of the surface with hydroxyls seems not do be a favored state. Neither dosing 1, 2, or 5 Langmuir, nor heavy bombardment with atomic hydrogen leads to an increase of observed hydroxyls. Besides forming of single hydroxyls, the surface becomes only slightly disordered and the basic structure remains intact after dosing hydrogen.

5 Summary and Outlook

The thesis consists of a detailed comparison of differently grown indium oxide single crystals via AES, Hall measurements, ICP-MS, LEIS, and STM and analysis of the $In_2O_3(001)$ surface under varying environment via LEED, STM, and XPS.

The most vital information was obtaining the amount and the species of residual elements for crystals grown in different fluxes. Comparing these to the physical properties found by other analysis methods point to their fundamental causes. High optical transparency and a yellowish color is found in samples with magnesium residues and either the presence of lead or the absence of platinum is responsible for a particular surface stoichiometry (at least in reducing environments).

Hall measurements revise the charge carrier concentration for crystal 8 from $n = 1 \times 10^{12}$ cm^{-3} to $n \approx 3 \times 10^{14}$ cm^{-3} and the carrier mobility to ≈ 0.2 cm^2·V^{-1}·s^{-1}. These results are not as extreme as the results in the preceding thesis, but show still a large deviation from previous values. Astounding are the values for two other samples. Though sharing similar composition, they show carrier concentrations in the range of 10^{18} cm^{-3} which is in the order of magnitude of previously accepted values. This shows a strong significance of minor changes in sample impurities.

STM investigation reveals further information on the surface structure of $In_2O_3(001)$. In reducing environment, atomic resolution of the underlying plane shows a 3.6 Å lattice in [110] direction. The structure suggests it to be the D-layer. The 2.5 Å high protrusions cannot simply consist of a half-filled M-layer [8] for two reasons: Only about half of the necessary atoms are observed and they are situated close to the same lattice sites as the underlying plane, while M-layer lattice atoms should sit between these sites.

Oxidizing the surface leads to an increase of surface oxygen, although indium remains dominating according to LEIS. STM images show a heavily disturbed surface and very rough terraces. No atomic resolution could be obtained due to difficult scanning conditions. Dosing hydrogen, both, in form of heavy bombardment with atomic H or surface exposure to D_2O of a few Langmuir has no severe effect. A few single hydroxyls form on the surface, which can be removed by heating the sample to at least 300°C.

Future investigations should contain further conductivity measurements for different samples and carefully linking the results to the sample composition obtained by ICP-MS. This information can help to grow even better

samples hopefully recreating or even exceeding the quality of batch 8. These samples should then be investigated by STM and compared to previous results and theoretical calculations. Also further investigation of the surface in oxidized environment is needed because it is the preferred state outside of vacuum.

6 Acknowledgements

I wish to thank Prof. Ulrike Diebold for excellent supervision. Her way of staying close to the group and visiting every single student as often as possible for checking and discussing their work (not avoiding sitting down and sharing the sometimes painful experience of finetuning an STM image) is unique for a person occupied with countless duties. I felt welcome and my input was always very much appreciated for which I am truly grateful.

Also I wish to thank Prof. Michael Schmid for patient answering many experimental and theoretical questions, which helped me a lot in understanding the physics behind my research, Peter Jackson for keeping the system running when I had troubles, and Daniel Hagleitner whose work I continued and who supported me with many useful informations. In fact, every member of the group was very helpful and it has been a pleasure to work in such an international environment.

Furthermore I wish to express my gratitude and admiration to the austrian students union. The commitment of these countless students, who spend countless hours working and fighting for improvents of study conditions cannot be appreciated enough. For me personally, it also meant finding a second home, gaining experience outside my study topic, and meeting a lot of interesting people, some of those I consider now good friends.

The greatest thanks go out to my family. They supported me throughout my study without any word of doubt, even when I took a slight detour to student politics and there was not much progress in my study for a few semesters. Finally, there is my girlfriend Carina, who not only helped me with many physical problems, but also always found the right words when I needed to be cheered up. Thank you.

References

[1] D. Hagleitner. Bulk and surface characterization of In_2O_3(001) single crystals. Master's thesis, Vienna University of Technology, 2011.

[2] Daniel Hagleitner. Project work: Surface properties of indium oxide (100) single crystals, 2011.

[3] A. Walsh, C. Richard, and A. Catlow. Structure, stability and work functions of the low index surfaces of pure indium oxide and Sn-doped indium oxide (ITO) from density functional theory. *J. Mater. Chem.*, 20(46):10438, 2010.

[4] T. Bielz, H. Lorenz, W. Jochum, R. Kaindl, F. Klauser, B. Klötzer, and Simon Penner. Hydrogen on In_2O_3: Reducibility, bonding, defect formation, and reactivity. *The Journal of Physical Chemistry C*, 114(19):9022–9029, 2010.

[5] V. Golovanov, Matti A. Mäki-Jaskari, Tapio T. Rantala, G. Korotcenkov, V. Brinzari, A. Cornet, and J. Morante. Experimental and theoretical studies of indium oxide gas sensors fabricated by spray pyrolysis. *Sensors and Actuators B: Chemical*, 106(2):563–571, 2005.

[6] P. D. C. King, T. Veal, D. Payne, A. Bourlange, R. Egdell, and C. McConville. Surface electron accumulation and the charge neutrality level in In_2O_3. *Physical Review Letters*, 101(11):116808, 2008.

[7] P. W. Tasker. The stability of ionic crystal surfaces. *Journal of Physics C: Solid State Physics*, 12(22):4977, 1979.

[8] P. Agoston and K. Albe. Thermodynamic stability, stoichiometry, and electronic structure of bcc-In_2O_3 surfaces. *Phys. Rev. B*, 84:045311, 2011.

[9] P. D. C. King, T. D. Veal, F. Fuchs, Ch. Y. Wang, D. J. Payne, A. Bourlange, H. Zhang, G. R. Bell, V. Cimalla, O. Ambacher, R. G. Egdell, F. Bechstedt, and C. F. McConville. Band gap, electronic structure, and surface electron accumulation of cubic and rhombohedral In_2O_3. *Phys. Rev. B*, 79:205211, 2009.

[10] E. H. Morales, Y. He, M. Vinnichenko, B. Delley, and U. Diebold. Surface structure of Sn-doped In_2O_3(111) thin films by STM. *New Journal of Physics*, 10(12):125030, 2008.

[11] E. H. Morales and U. Diebold. The structure of the polar Sn-doped indium oxide (001) surface. *Applied Physics Letters*, 95(25):253105, 2009.

[12] A. Bourlange, D.J. Payne, R.G. Palgrave, J.S. Foord, R.G. Egdell, R.M.J. Jacobs, A. Schertel, J.L. Hutchison, and P.J. Dobson. Investigation of the growth of In_2O_3 on Y-stabilized ZrO_2(100) by oxygen plasma assisted molecular beam epitaxy. *Thin Solid Films*, 517(15):4286–4294, 2009.

[13] D. Hagleitner, M. Menhart, P. Jacobson, S. Blomberg, K. Schulte, E. Lundgren, M. Kubicek, J. Fleig, F. Kubel, C. Puls, A. Limbeck, H. Hutter, L. A. Boatner, M. Schmid, and U. Diebold. Bulk and surface characterization of In_2O_3(001) single crystals. *Phys. Rev. B*, 2012.

[14] J. P. Remeika and E. G. Spencer. Electrical conductivity and growth of single-crystal indium sesquioxide. *Journal of Applied Physics*, 35(10):2803–2803, 1964.

[15] P. Agoston and K. Albe. Ab initio modeling of diffusion in indium oxide. *Phys. Rev. B*, 81:195205, 2010.

[16] M. Marezio. Refinement of the crystal structure of In_2O_3 at two wavelengths. *Acta Crystallographica*, 20(6):723–728, 1966.

[17] R.D. Shannon. New high pressure phases having the corundum structure. *Solid State Communications*, 4(12):629–630, 1966.

[18] A. Nørlund Christensen, N. C. Broch, O. von Heidenstam, and Å. Nilsson. Hydrothermal investigation of the systems In_2O_3-H_2O-Na_2O and In_2O_3-D_2O-Na_2O. the crystal structure of rhombohedral In_2O_3 and of $In(OH)_3$. *Acta Chemica Scandinavica*, 21:1046–1056, 1967.

[19] J. Chenavas J. J. Capponi M. Marezio A. Waintal and M. Gondrand. *Colloq. Int. Centr. Nat. Rech. Sci.*, 188:403, 1970.

[20] J.H.W. De Wit. Structural aspects and defect chemistry in In_2O_3. *Journal of Solid State Chemistry*, 20(2):143–148, 1977.

[21] G. Korotcenkov, V. Brinzari, A. Cornet, and J. Morante. Experimental and theoretical studies of indium oxide gas sensors fabricated by spray pyrolysis. *Sensors and Actuators B: Chemical*, 106(2):563–571, 2005.

[22] C. Zhou, J. Li, S. Chen, J. Wu, K. R. Heier, and H. Cheng. First-principles study on water and oxygen adsorption on surfaces of indium oxide and indium tin oxide nanoparticles. *The Journal of Physical Chemistry C*, 112(36):14015–14020, 2008.

[23] R. L. Weiher. Electrical properties of single crystals of indium oxide. *Journal of Applied Physics*, 33(9):2834–2839, 1962.

[24] J.H.W. De Wit. Electrical properties of In_2O_3. *Journal of Solid State Chemistry*, 8(2):142–149, 1973.

[25] J.H.W. de Wit. The high temperature behavior of In_2O_3. *Journal of Solid State Chemistry*, 13(3):192–200, 1975.

[26] G. Frank and H. Köstlin. Electrical properties and defect model of tin-doped indium oxide layers. *Applied Physics A Solids and Surfaces*, 27:197–206, 1982.

[27] T. Tomita, K. Yamashita, Y. Hayafuji, and H. Adachi. The origin of n-type conductivity in undoped In_2O_3. *Applied Physics Letters*, 87(5):051911, 2005.

[28] S. Lany and A. Zunger. Dopability, intrinsic conductivity, and nonstoichiometry of transparent conducting oxides. *Phys. Rev. Lett.*, 98:045501, 2007.

[29] J. R. Bellingham, W. A. Phillips, and C. J. Adkins. Electrical and optical properties of amorphous indium oxide. *Journal of Physics: Condensed Matter*, 2(28):6207, 1990.

[30] Michael Schmid. Lecture Notes: Experimentelle Methoden der Oberflächenphysik, TU Wien, 2011.

[31] B. Stöger. Surface defects of graphene grown on Ni(111). Master's thesis, Vienna University of Technology, 2011.

[32] Peter Varga. Lecture Notes: Physikalische Analytik, TU Wien, 2004.

[33] P. Auger. Sur les rayons β secondaires produits dans un gaz par des rayons X. *C.R.A.S. 177*, 177:169–171, 1923.

[34] L. Meitner. Über die Entstehung der β-Strahl-Spektren radioaktiver Substanzen. *Zeitschrift fur Physik*, 9:131–144, 1922.

[35] W. Demtröder. *Experimentalphysik 2: Elektrizität und Optik (Springer-Lehrbuch) (German Edition)*. Springer, 2 edition, 2002.

[36] L. J. Van Der Pauw. A method of measuring specific resistivity and Hall effect of discs of arbitrary shape. *Philips Research Reports*, 13(1):1–9, 1958.

[37] L. J. Van Der Pauw. A method of measuring the resistivity and Hall coefficient on lamellae of arbitrary shape. *Philips Technical Review*, 20(8):220–224, 1958.

[38] H. Haraguchi, T. Hasegawa, and M. Abdullah. Inductively coupled plasmas in analytical atomic spectrometry: excitation mechanisms and analytical feasibilities. *Pure Appl. Chem.*, Vol. 60(No. 5, pp.):685–696, 988.

[39] R. E. Wolf. What is ICP-MS? ... and more importantly, what can it do? *Research Chemist*, 2005.

[40] H. Lüth. *Surfaces and interfaces of solids*. Springer series in surface sciences. Springer-Verlag, 1993.

[41] N. W. Ashcroft and D. N. Mermin. *Solid State Physics*. Thomson Learning, Toronto, first edition, 1976.

[42] W. Demtröder. *Experimentalphysik 3: Atome, Moleküle und Festkörper (Springer-Lehrbuch) (German Edition)*. Springer, 3., überarb. aufl. edition, 2005.

[43] J. Tersoff and D. R. Hamann. Theory of the scanning tunneling microscope. *Phys. Rev. B*, 31:805–813, 1985.

[44] J. Bardeen. Tunnelling from a many-particle point of view. *Phys. Rev. Lett.*, 6:57–59, 1961.

[45] G. Binnig, H. Rohrer, C. Gerber, and E. Weibel. Tunneling through a controllable vacuum gap. *Applied Physics Letters*, 40(2):178–180, 1982.

[46] G. Binnig, H. Rohrer, Ch. Gerber, and E. Weibel. Surface studies by scanning tunneling microscopy. *Phys. Rev. Lett.*, 49:57–61, 1982.

[47] A. Einstein. Eine neue Bestimmung der Moleküldimensionen. *Ann. Phys.*, 324(2):289–306, 1906.

[48] VG Microtech. *Dual Anode X-ray Sources Systems Operating Manual*.

[49] I. Mills, C. Tomislav, K. Homann, K. Nikola, and K. Kuchitsu, editors. *Quantities, Units and Symbols in Physical Chemistry*. Blackwell Science, Cambridge, second edition, 1993.

[50] L. E. Davis, N. C. MacDonald, P. W. Palmberg, G. E. Riach, and R. E. Weber. *Handbook of Auger electron spectroscopy : a reference book of standard data for identification and interpretation of Auger electron spectroscopy data*. Physical Electronics Industries, 1976.

[51] C. Kittel. *Introduction to Solid State Physics*. John Wiley and Sons (WIE), eighth edition, 2004.

[52] E. Morales. *Growth and surface characterization of tin-doped indium oxide thin films*. PhD thesis, Tulane University School of Science and Engineering, 2010.

[53] J. T. Kloprogge, L. V. Duong, B. J. Wood, and R. L. Frost. XPS study of the major minerals in bauxite: Gibbsite, bayerite and (pseudo)boehmite. *Journal of Colloid and Interface Science*, 296(2):572–576, 2006.

List of Figures

List of Tables

A Appendix

#	In_2O_3 [g]	B_2O_3 [g]	PbO [g]	additive	Mol %	Treatment	Color
1	1.388	1.392	16.127	0.154 g CaO	2.75	0	green black
2a	2	2	25	0.1244 g CaO	1.5	0	green black
2b	2	2	25	0.124 g CaO	1.5	0	green black
2c	1.388	1.392	16.18	0.140 g CaO	2.5	0	green black
3	1.388	1.392	16.127	0.110 g MgO	2.75	0	yellow
4a	1.388	1.392	16.182	0.101 g MgO	2.5	0	yellow
4b	1.388	1.392	16.182	0.101 g MgO	2.5	0	yellow
4c	1.388	1.392	16.127	0.1108 g MgO	2.5	heated to 1250°C	yellow
5a	1.388	1.392	16.405	0.0646 g MgO	1.5	0	yellow
5b	2	2	25	0.0895 g MgO	1.5	0	dark yellow
5c	1.388	1.392	16.405	0.0646 g MgO	1.5	0	yellow green
5d	2	2	25	0.08942 g MgO	1.5	0	green
5e	2	2	25	0.08942 g MgO	1.5	0	yellow green
5f	2.226	2.784	32.81	0.1292 g MgO	1.5	0	yellow
5g	2.226	2.784	32.7002	0.14106 g MgO	1.5	0	yellow
6a	2	2	25	-	-	0	green
6b	2	2	25	-	-	0	green black
6c	2	2	25	-	-	O2;12 hours@1050°C	black
6d	2	2	25	-	-	0	green black
7	2	2	25	0.3402 g BaO	1.5	0	green black
8	?	?	?	?	?	?	yellow
9	?	?	?	MgO	1.5	O2;36 hours@1110°C; Vac; 66 hours@1050°C	yellow

Table A.1: List of crystals, their growth components and treatment

Date	Numbers	Sputtering	Annealing	T [°C]	Dosing	Surface
09/21/11	1001-1025	15 min (2 cycles)	10 min (2 cycles)	500	-	clean
09/29/11	1026-1033	15 min (2 cycles)	10 min (2 cycles)	500	oxygen, ThC, 40W, 2.4e-7mbar, 30 min	oxidized
09/30/11	1034-1042	-	-	-	-	oxidized
10/03/11	1043-1057	15 min (3 cycles)	10 min (3 cycles)	500	-	clean
10/05/11	1058-1068	15 min (3 cycles)	10 min (3 cycles)	500	oxygen, ThC, 40W, 2.5e-7mbar, 30 min	oxidized
10/06/11	1069-1073	-	-	-	-	oxidized
10/07/11	1074-1107	15 min (3 cycles)	10 min (3 cycles)	500	-	clean
10/10/11	1108-1119	15 min (3 cycles)	10 min (3 cycles)	500	oxygen, ThC, 40W, 2.4e-7mbar, 300°C, 30 min	oxidized
10/11/11	1120-1155	-	-	-	-	oxidized
10/13/11	1156-1169	15 min (3 cycles)	10 min (3 cycles)	500	oxygen, ThC, 50W, 2.4e-7mbar, 300°C, 30 min	oxidized
10/19/11	1170-1182	15 min	10 min	500	-	clean
10/19/11	1183-1189	1 h, 15 min	15 min, 10 min	500	-	clean
10/20/11	1190-1191	30 min	10 min	500	-	clean
10/20/11	1192-1219	-	-	-	oxygen, ThC, 50W, 2.3e-7mbar, 300°C, 30 min	oxidized
10/21/11	1220-1246	-	-	-	-	oxidized
10/24/11	1247-1266	15 min (3 cycles)	10 min (3 cycles)	500	-	clean
10/27/11	-	15 min (3 cycles)	10 min (3 cycles)	500	oxygen, ThC, 50W, 2.4e-7mbar, 20 min @ 300°C, 10 min @ 500°C	oxidized
10/28/11	1267-1281	-	-	-	-	oxidized
10/31/11	1282-1303	15 min (3 cycles)	10 min (3 cycles)	500	-	clean
11/02/11	1304-1332	15 min (3 cycles)	10 min (3 cycles)	500	-	clean
11/03/11	1333-1364	15 min (2 cycles)	10 min (2 cycles)	500	oxygen, ThC, 50W, 2.5e-7mbar, 20 min @ 300°C, 10 min @ 500°C	oxidized
11/04/01	1365-1398	-	-	-	-	oxidized

11/07/11	1399-1419	15 min (3 cycles)	10 min (3 cycles)	500	-	clean
11/08/11	1420-1443	15 min (2 cycles)	10 min (2 cycles)	500	oxygen, ThC, 50W, 2.5e-7mbar, 20 min @ 300°C, 10 min @ 500°C	oxidized
11/09/11	1444-1473	-	-	-	-	oxidized
11/09/11	1474-1492	-	5 min	500	-	oxidized
11/10/11	1493-1514	-	-	-	-	oxidized
11/14/11	-	15 min (3 cycles)	10 min (3 cycles)	500	oxygen, ThC, 50W, 2.4e-7mbar, 20 min @ 300°C, 10 min @ 500°C	oxidized
11/15/11	1515-1557	-	-	-	-	oxidized
11/21/11	1558-1587	15 min (3 cycles)	10 min (3 cycles)	500	-	clean
11/22/11	1588-1629	15 min (3 cycles)	10 min (3 cycles)	500	-	clean
11/23/11	-	15 min (3 cycles)	10 min (3 cycles)	500	oxygen, ThC, 50W, 2.4e-7mbar, 20 min @ 300°C, 10 min @ 500°C	oxidized
11/24/11	1630-1647	-	10 min	500	-	oxidized
11/25/11	1648-1684	-	10 min	500	-	oxidized
11/28/11	1685-1714	15 min (3 cycles)	10 min (3 cycles)	500	-	clean
12/02/11	1715-1724	15 min (2 cycles)	10 min (2 cycles)	500	hydrogen, ThC, 50W, 2.4e-7mbar, 20 min ramp to 500°C, 20 min @ 500°C	hydrogenated
12/05/11	1725-1757	15 min (3 cycles)	10 min (3 cycles)	500	-	clean
12/06/11	1758-1808	15 min (3 cycles)	10 min (3 cycles)	500	hydrogen, ThC, 50W, 2.4e-7mbar, 30 min @ 500°C	hydrogenated
12/07/11	1809-1323	15 min (3 cycles)	10 min (3 cycles)	500	hydrogen, ThC, 50W, 2.4e-7mbar, 30 min	hydrogenated
12/09/11	1824-1851	15 min (3 cycles)	10 min (3 cycles)	500	-	clean
12/12/11	1852-1881	15 min (3 cycles)	10 min (3 cycles)	500	hydrogen, ThC, 50W, 2.4e-7mbar, 30 min @ 500°C	hydrogenated
12/15/11	1882-1908	15 min (3 cycles)	10 min (3 cycles)	500	-	clean
12/16/11	1909-1931	15 min (3 cycles)	10 min (3 cycles)	500	-	clean

01/16/12	1932-1942	15 min (4 cycles)	10 min (3 cycles)	500	D_20 Evaporation: 100s, 5e-8mbar = 5 L, annealing at 500°C	water dosed
01/17/12	1943-1963	15 min (3 cycles)	10 min (2 cycles)	500	D_20 Evaporation: 100s, 5e-8mbar = 5 L, annealing at 500°C	water dosed
01/18/12	1964-1976	15 min (3 cycles)	10 min (3 cycles)	500	D_20 Evaporation: 100s, 5e-8mbar = 5 L	water dosed
01/19/12	1977-2010	15 min (3 cycles)	10 min (3 cycles)	500	D_20 Evaporation: 20s, 5e-8mbar = 1 L	water dosed
01/23/12	2011-2046	15 min (3 cycles)	10 min (3 cycles)	500	D_20 Evaporation: 20s, 5e-8mbar = 1 L	water dosed
01/24/12	2047-2057	15 min (3 cycles)	10 min (3 cycles)	650/500	-	clean
01/24/12	2058-2066	-	-	-	D_20 Evaporation: 40s, 5e-8mbar = 2 L	water dosed
01/25/12	2067-2087	15 min (2 cycles)	10 min (2 cycles)	500	D_20 Evaporation: 40s, 5e-8mbar = 2 L	water dosed
01/25/12	2088-2099	-	flashing	300	-	water dosed
01/30/12	2100-2105	15 min (3 cycles)	10 min (3 cycles)	500	-	clean
01/31/12	2106-2109	15 min (3 cycles)	10 min (3 cycles)	500	oxygen, ThC, 50W, 2.4e-7mbar, 20 min @ 300°C, 10 min @ 500°C	oxidized

Table A.2: Overview of STM measurements